Anomalous Crystalline-Electromagnetic Responses in Semimetals

Mark R. Hirsbrunner,[1,*] Oleg Dubinkin,[1,*] F. J. Burnell,[2] and Taylor L. Hughes[1]
[1]Department of Physics and Institute of Condensed Matter Theory, University of Illinois at Urbana-Champaign, Urbana, Illinois 61801, USA
[2]Department of Physics, University of Minnesota Twin Cities, Minnesota 55455, USA

(Received 1 May 2024; revised 7 September 2024; accepted 4 October 2024; published 9 December 2024)

We present a unifying framework that allows us to study the mixed crystalline-electromagnetic responses of topological semimetals in spatial dimensions up to $D = 3$ through dimensional augmentation and reduction procedures. We show how this framework illuminates relations between the previously known topological semimetals and use it to identify a new class of quadrupolar nodal line semimetals for which we construct a lattice tight-binding Hamiltonian. We further utilize this framework to quantify a variety of mixed crystalline-electromagnetic responses, including several that have not previously been explored in existing literature, and show that the corresponding coefficients are universally proportional to weighted momentum-energy multipole moments of the nodal points (or lines) of the semimetal. We introduce lattice gauge fields that couple to the crystal momentum and describe how tools including the gradient expansion procedure, dimensional reduction, compactification, and the Kubo formula can be used to systematically derive these responses and their coefficients. We further substantiate these findings through analytical physical arguments, microscopic calculations, and explicit numerical simulations employing tight-binding models.

DOI: 10.1103/PhysRevX.14.041060 Subject Areas: Condensed Matter Physics

I. INTRODUCTION

Topological responses are a key manifestation of electronic topology in solids. Celebrated examples such as the integer quantum Hall effect [1–3] and axion electrodynamics [4,5] have paved the way for a broader exploration of topological response phenomena in insulating systems. As of now, a wide variety of phenomena that are directly determined by the electronic topology have been considered, including thermal response [6,7], geometric response [8–24], and electric multipole response [25–27]. These responses are robust features of topological insulators (TIs) and topological phases, in general, and are often described by a quantized response coefficient, e.g., the integer Hall conductance [1–3] or the quantized magnetoelectric polarizability [5,28,29].

Interestingly, certain distinctive features of response of topological Weyl or Dirac semimetals can be described by response theories that are closely analogous to those of topologically insulating phases, albeit with coefficients that are determined by the momentum-space and energy locations of the point or line nodes [30–35]. For point-node semimetals, the relevant response coefficients are momentum-energy vectors determined as a sum of the momentum and energy locations of the point nodes weighted by their chirality (or by their helicity, for Dirac semimetals), yielding a momentum-energy space dipole. For example, the low-energy, nodal contribution to the anomalous Hall effect tensor of a 3D Weyl semimetal is determined by the momentum components of this momentum-energy dipole vector.

The quasitopological response coefficients of topological semimetals are not strictly quantized, since they can be continuously tuned with the nodal momenta. However, the forms of the responses share many features with topological insulators in one lower dimension or, perhaps more precisely, with weak topological insulators in the same dimension [36,37]. Indeed, topological semimetals and weak topological insulators both require discrete translation symmetry to be protected, and both are sensitive to translation defects such as dislocations [38]. Interestingly, the connection to translation symmetry has motivated recent work which recasts many previously proposed topological responses of these systems as couplings between the electromagnetic gauge field A_μ and gauge fields for translations a_μ, where μ runs over spacetime indices and a runs over the spatial directions in which translation symmetry exists. This insight has also led to the

*These authors contributed equally to this work.

development of new response theories that are just beginning to be understood [17–20,24].

Motivated by these previous results and our recent related work on higher-rank chiral fermions [17,24,39], here we study the topological responses of 1D, 2D, and 3D topological semimetals coupled to electromagnetic and strain (translation gauge) fields. In addition to the well-studied dipole case mentioned above, we also study cases where point nodes have momentum-energy quadrupole or octupole patterns. Our approach allows us to make clear connections between a wide variety of response theories across dimensions and clarifies relationships between many of the response theories we discuss. We find that the chirality-weighted momentum-energy multipole moments of the semimetals determine new types of quasitopological responses to electromagnetic fields and strain. We are able to explicitly derive many of these responses from Kubo formula calculations (sometimes combined with dimensional reduction procedures [5]). Using these results, we explicitly study these families of response theories using lattice model realizations. We also extend our results to the responses of nodal line semimetals (NLSMs) and construct a new type of NLSM with an unusual crossed, cagelike nodal structure.

Generically, topological semimetals are robust only in the presence of both translation and charge conservation symmetry. As such, we focus here on response theories built from gauge fields for these two ubiquitous symmetries. Recently, there has been considerable interest in topological semimetals protected by a variety of crystalline symmetries. Examples include type-I Dirac semimetals protected by discrete rotation symmetry and exotic semimetals with three-, four-, six-, and even eightfold band crossings protected by nonsymmorphic crystalline symmetries [40,41]. Additional internal symmetries beyond charge conservation, such as chiral symmetry, are also often required to protect the nodal Fermi surfaces in many cases [42–44]. Combinations of internal and point group symmetry can also play a key role, with some examples being nodal-line topological semimetals carrying Z_2 monopole charge and nodal-surface topological semimetals protected by spacetime inversion symmetry [44–47]. In many of these examples, interesting responses involving these additional symmetries are likely to occur in addition to what we study here. Indeed, there has been a wide range of recent work in 2D and 3D studying responses of insulators and semimetals to gauge fields of discrete rotation symmetry [18,48–52]. While a full discussion of all possible responses is beyond the scope of our work, our general approach can be applied to study cases having more complicated symmetry protection. We comment in the conclusion on possible future directions for response theories involving symmetries beyond translation and U(1) charge conservation.

Our article is organized as follows. In Sec. II, we provide an overview of and intuition about the response theories that are discussed in more detail, and in model contexts, in later sections. In Sec. III, we derive a family of effective actions that describe mixed crystalline-electromagnetic responses in various spatial dimensions. From here, we proceed in Sec. IV by presenting concrete lattice models and explicit numerical calculations that realize and demonstrate the mixed responses in $D = 1, 2, 3$. We conclude in Sec. V by discussing possible extensions to future work and potential pathways to experimental observation of some of the described phenomena.

II. OVERVIEW OF RESPONSE THEORIES

The systems we consider in this article all exhibit U(1) charge conservation and discrete translation symmetry in at least one spatial direction. In the presence of these symmetries, we can consider the responses to background field configurations of the electromagnetic gauge field A_μ and a collection of translation gauge fields e^a_μ. For example, if the system exhibits translation symmetry in the x direction, then we can consider coupling the system to the field e^x_μ. Our goal is to study low-energy response theories of electrons coupled to translation and electromagnetic gauge fields.

Since most readers are likely less familiar with the translation gauge fields e^a_μ than the electromagnetic field A_μ, we briefly review the nature of these fields as they appear in our work. In a weakly deformed lattice, e^a_i is given by

$$e^a_j = \delta^a_j - \frac{\partial u^a}{\partial x^j}; \tag{1}$$

where the Kronecker δ^a_j encodes the fixed reference lattice vectors, u^a is the lattice displacement, and $\partial u^a/\partial x^j$ is the distortion tensor [53]. The fields e^a_j in Eq. (1) are reminiscent of gauge fields (see, e.g., Ref. [54]): From Eq. (1), we immediately see that line integrals of e describe lattice dislocations, since $\oint \partial_i u_a \, dx^i = b^a$, where b^a is the net Burgers vector of all the dislocations inside the loop [53]. This points to an analogy with the configurations of the usual electromagnetic field. The analog of magnetic fields derived from e^a_μ essentially encodes configurations of dislocations, each with an amount of flux equal to the corresponding Burgers vector. Additionally, electric fields are time-dependent strains. In earlier work, e.g., Ref. [11], these fields could have been called frame fields, but crucially the translation gauge fields encode only the translation or torsional part of the geometric distortion, whereas the frame fields also carry rotational information. In keeping with previous literature, here we call the set of (Abelian) fields e^a_μ translation "gauge" fields, by analogy of their relationship to translation "fluxes" (i.e., lattice defects). This language is convenient because, as we see, actions describing the response to such lattice fluxes are

invariant under (vector-charge) gauge transformations of the e^a_μ fields.

A second way in which we use the close analogy between e^a_μ and electromagnetic gauge fields is through the lattice analog of the usual Aharonov-Bohm effect (holonomy), in which a charged particle encircles a magnetic flux of the gauge field. In the electromagnetic case, a charged particle moving around a magnetic flux generates a U(1) phase factor. For the translation gauge field, taking a particle around a translation magnetic flux having Burgers vector b generates a translation operator by the displacement b^a. For particles with a fixed translation charge, i.e., a fixed momentum, this generates a momentum-dependent U(1) phase factor. This will lead us to introduce momentum-dependent Peierls factors when performing some lattice calculations. To complement this discussion, in Appendix A we show more explicitly how translation symmetry can be "gauged" under a teleparallel constraint of the underlying system geometry. A very similar approach has been used to study the effects of strain on graphene [55–57] and other semimetallic systems [58–62], where strain can play the role of a valley-dependent magnetic field.

For our purposes, there are many ways in which e^a_μ can be treated on equal footing with the electromagnetic gauge field. However, there are some important distinctions. First, the fields e^a_j in Eq. (1) are not true gauge fields. This becomes important when considering the possible response actions: While the total charge of a system strictly conserved, momentum conservation is not similarly inviolable (see, e.g., Refs. [60–62] for some interesting physical consequences of this distinction). Second, responses involving e^a_μ are predicated on the existence of translation symmetry. Thus, if the response is characterized by a boundary effect or a response to a flux or defect, we must be careful to ensure that (at least approximate) translation symmetry is maintained in order to connect the coefficient of the response action to explicit model calculations. Indeed, some responses are not well defined unless configurations that maintain translation symmetry are used. This is unlike the electromagnetic response for which U(1) charge symmetry is maintained independently of the geometry and gauge field configuration. Other important distinctions have been discussed in recent literature that has begun putting the gauging of discrete spatial symmetries on firmer ground [49,63,64]. One important distinction is that the translation gauge fields correspond to a discrete gauge symmetry $\mathbb{Z}_{N_a}$, where N_a is the number of unit cells in the ath direction. This discreteness can play an important role in the topological response properties [18], but we do not focus on this aspect in our work.

Using this framework, our goal is to consider the low-energy responses of electrons to the background electromagnetic and translation gauge fields. Given a translationally invariant Bloch Hamiltonian H, the response theories we consider can, in principle, be derived from correlation functions of the electromagnetic current

$$j^\mu = e\frac{\partial H}{\partial k_\mu} \tag{2}$$

and the crystal momentum current

$$J^\mu_a = \hbar k_a \frac{\partial H}{\partial k_\mu}; \tag{3}$$

where the former couples to A_μ and the latter to e^a_μ (see Appendix A for more details for the latter). Indeed, we take exactly this approach in Sec. III to derive response actions for 2D and 3D systems. While our explicit derivations are important for precisely determining the coefficients of the response actions we study, it is helpful to first motivate the overarching structure that connects a large subset of these response theories. We also note that alternative approaches to determining some of the response actions we discuss have been proposed in Refs. [18–20], and, where the results overlap with ours, they agree.

To understand the connections between the response theories we study, it is useful to begin by reviewing the well-known dimensional hierarchy of response theories of strong topological insulators [5]. We show the general structure in Fig. 1(a), where the response terms are built solely from the electromagnetic gauge field. Furthermore, Chern-Simons and θ-term response actions appear in even and odd spatial dimensions, respectively. There are a number of connections between the theories in different dimensions, and we now review three of them. First, a Chern-Simons action in D spatial dimensions can be dimensionally reduced to a θ-term action in $(D-1)$ dimensions by compactifying one spatial direction [65,66]. The $(D-1)$-dimensional system can also represent a TI if the value of θ is quantized to be 0; π by a symmetry that protects the $(D-1)$-dimensional topological insulator [5]. Second, one can consider the reverse process where quantized adiabatic pumping [67] in $(D-1)$ dimensions will convert a θ-term action to a D-dimensional Chern-Simons action. Finally, a θ-term action for a $(D-1)$-dimensional topological insulator exhibits a half-quantized $(D-2)$-Chern-Simons response on boundaries where θ jumps by π. These general relationships are summarized in Fig. 1(a), where each type of relationship is color and symbol coordinated.

Next, we can consider a less familiar set of relationships in Fig. 1(b) between gapped theories with mixed crystalline-electromagnetic responses arising from effective actions having both A_μ and e^a_μ fields. We emphasize that the precise relationships we refer to in Fig. 1(b) are for gapped systems where the coefficients of the actions are quantized. In contrast, for the majority of this article, we focus on the quasitopological responses of gapless systems which take

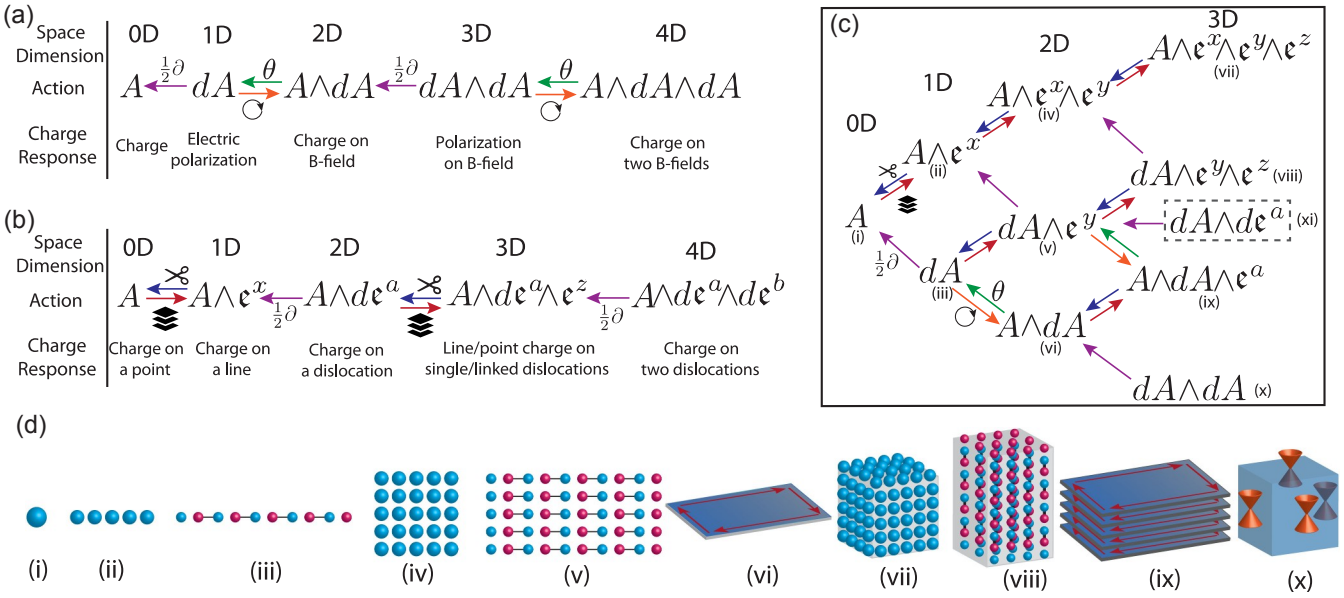

FIG. 1. (a) A dimensional hierarchy of theories describing responses of strong topological insulators. The theories are related by dimensional reduction (θ symbol, green arrow) [5], taking the boundary response [$\delta 1 = 2\pi\partial$ symbol, purple arrow], or adiabatic pumping (↻ symbol, red arrow) [67]. (b) A dimensional hierarchy of insulating systems with mixed crystalline-electromagnetic responses. The theories are related by stacking (layer symbol, dark red arrow) and cutting (scissor symbol, blue arrow). (c) A family tree of dimensional hierarchies establishing connections between responses of strong TIs and insulators with mixed crystalline-electromagnetic responses. (d) Illustrations representing the nature of the phases constituting the hierarchy depicted in (c). (i) A single isolated charge. (ii) A line of charges forming a lattice. (iii) An insulating chain having a quantized charge polarization. (iv) A two-dimensional lattice of charges. (v) A two-dimensional weak topological insulator where polarized chains are stacked transverse to their polarization. (vi) A two-dimensional Chern insulator having chiral edge states indicated by red arrows. (vii) A three-dimensional lattice of charges. (viii) A three-dimensional lattice built from a two-dimensional array of polarized chains; alternatively, a stack of two-dimensional weak topological insulators. (ix) A three-dimensional stack of Chern insulators forming a time-reversal-breaking weak topological insulator. (x) A three-dimensional strong topological insulator with surface Dirac cones.

similar forms, but with nonquantized coefficients. Remarkably, many of the actions we discuss for insulators can be generalized to the nonquantized case. For semimetals, however, the dimensional relationships we point out are more akin to physical guides than a precise prescription for deriving matching coefficients in between dimensions.

With this caveat in mind, let us consider the family of theories in Fig. 1(b). In 0D, we can consider the response action for a gapped system of electrons, $S = A\,Q_e = \theta N_e$, which represents a system with charge $Q = eN_e$, where N_e is the (integer) number of electrons. If we imagine stacking these 0D systems in a discrete, translationally invariant lattice in the x direction, then we generate a line of charges. Indeed, stacking produces the response for a translation-invariant line-charge density which is captured by the next action in the sequence in Fig. 1(b), i.e., $Q = \int A \wedge e^x = Q \int dx dt(A_0 e^x_x - A_x e^x_0)$. In this action, the first term represents the charge density along the line, while the second term represents a current generated if the lattice of charges is moving. The latter consequence becomes manifest in the weakly distorted lattice limit, since the currents proportional to the displacement rate: $j^x \sim e^x_0 \sim \delta\partial u^x/\partial t$.

We can also imagine a reverse process where we are given a translationally invariant line of charge at integer filling and cut out a single unit cell. Since the system is gapped and translation invariant, this results in a move in the opposite direction in Fig. 1(b), i.e., from A^x in 1D to A in 0D with the same integer coefficient Q. We can use this example to highlight our caveat about gapped vs gapless systems mentioned above. That is, while it is reasonable to have a 1D gapless system with nonquantized (i.e., noninteger) charge (per unit cell) described by the 1D action, the cutting procedure does not work properly at noninteger filling, since the result will be a 0D point with a fractional charge.

In comparison to the response sequence for strong TIs, we see that stacking is the analog of pumping for the translation gauge field [68]. Indeed, while pumping adds an extra electromagnetic gauge field factor A, stacking adds an extra translation gauge field factor $e^{D\neq 1}$, where $D \neq 1$ is the stacking direction. As a result, given any action in the strong TI sequence, we can stack copies to get the response action of a primary weak TI (stacks of codimension-1 strong TIs, e.g., lines stacked into 2D) by adding a wedge

product with $e^{Dþ1}$. We can push the stacking idea further to generate secondary weak TIs (stacks of codimension-2 strong TIs, e.g., lines stacked into 3D) by a wedge product with $e^{Dþ1} \wedge e^{Dþ2}$ and so on.

The stacking and cutting procedures are not the only relationships between the response theories in Fig. 1(b). Just as in the strong TI sequence, we can find connections between the boundary properties of some D-dimensional systems and the bulk response of a (D − 1)-dimensional system. For example, the 2D response action in Fig. 1(b) represents the response of a stack of Su-Schrieffer-Heeger (SSH) chains [69], each with a quantized polarization of e=2. The boundary of such a 2D system is a line of charge on the edge, albeit with a density of e=2 electrons per unit cell on the edge line instead of the integer density we would get by stacking integer-filled 0D points. As such, the boundary of the 2D $A \wedge de^x$ action represents a line charge described by the action $A \wedge e^x$, but with a half-integer coefficient.

Now we can combine the dimensional relationships in the sequences of both Figs. 1(a) and 1(b) to make a family tree of related theories. We show a tree in Fig. 1(c) that includes response actions in zero, one, two, and three spatial dimensions. In 0D, we have only an integer electron charge response that couples to A_0. For 1D, we can either stack charges to form a line of charge (upper branch) or consider an electrically polarized TI (lower branch) where the charge is split in half and moved to opposing ends of the chain while the interior remains neutral (so to speak). In 2D, we can stack line charges to get a plane of charge (top branch), stack 1D polarized TIs to get a weak TI (middle branch), or pump charge in a 1D TI to generate a 2D Chern insulator (bottom branch).

In 3D, the set of responses is richer. We can stack plane charges to generate a 3D volume of charges (top branch), stack Chern insulators to get a 3D primary weak TI (second from bottom branch), or stack 2D weak TIs to get a 3D secondary weak TI built from 1D polarized wires (second branch from top). The other well-known possibility is the magnetoelectric response for a 3D strong TI [5,28] (bottom branch). Although it is not shown, this theory is related to a 4D quantum Hall system via pumping (3D to 4D) or dimensional reduction (4D to 3D) [5]. The final option we consider, which is the middle branch enclosed by a dotted rectangle, is $\int dA \wedge de^a$. This response theory has not been previously studied in detail. This theory is a total derivative and yields a gapped boundary with an electric polarization (e.g., a stack of SSH chains on the boundary). This is reminiscent of an electric quadrupole (higher-order) response [27,70], and we explore this connection further in Sec. III E.

While this discussion has centered on gapped systems, our primary focus is on gapless topological semimetals. Importantly, each of the actions that contains a translation gauge field in the family tree in Fig. 1(c) can also represent a contribution to the response of various types of metals or topological semimetals [17–20,24,30–34]. This is because many semimetals can be generated by translation-invariant stacking of lower-dimensional topological phases. Since the momentum k_a in the stacking direction is conserved, one can consider adding up the set of topological response terms for each gapped k_a. A semimetal represents a scenario where the coefficients of these topological terms at each k_a are quantized and have discrete jumps where k_a hits a nodal point. For example, the 2D electric polarization response of a stack of 1D TIs becomes the response of a 2D Dirac semimetal if the wires forming the stack are coupled strongly enough to close the insulating gap [34]. In the presence of reflection symmetry, each momentum in the stacking direction has a quantized charge polarization that jumps when the momentum hits a gapless 2D Dirac point. Additionally, the 3D response of a stack of Chern insulators becomes the nonquantized anomalous Hall effect response of a time-reversal-breaking Weyl semimetal where each fixed-k plane that does not intersect a Weyl point carries a quantized Chern number that jumps at a Weyl point [30–33], and so on. While many of these response theories have been discussed in detail before, only a few works have highlighted the contributions from the translation gauge fields [12,17–20,24,71,72]. As such, a large fraction of our paper is devoted to both the explicit derivations of the response coefficients of the actions in Fig. 1(c) that have couplings to the translation gauge fields (Sec. III) and to the explicit calculations of the physical response phenomena in representative model systems (Sec. IV).

Before we move on to more explicit derivations, we want to motivate three additional response theories we study that lie outside the family tree in Fig. 1(c). As mentioned above, a remarkable feature of the response actions of point-node semimetals is that their coefficients are determined from the energy-momentum locations of the nodal points. Indeed, for the relevant response actions in Fig. 1(c), the coefficients are obtained as a chirality-weighted momentum dipole moment of the point nodes (note that Dirac points do not have a chirality; nevertheless, there is a signed quantity that plays the same role). Interestingly, recent work on rank-2 chiral fermions and Weyl semimetals with a chirality-weighted momentum quadrupole moment [17–19,24] has unveiled a new set of response theories. This category of theories has actions that include factors of more than one translation gauge field of the same type (e.g., $e^a \wedge de^b$, where a ¼ b) and, as such, does not appear in the family tree in Fig. 1(c). This also implies that the translation gauge field factors in these response theories cannot be obtained by the conventional stacking of lower-dimensional systems that we discuss above, since stacking produces wedge products with distinct translation gauge fields. We could also construct related higher-dimensional theories (and lower-dimensional theories if we consider

both space and time translational gauge fields) to form an additional connected tree of theories, but we leave further discussion of those extensions to future work.

To give some explicit examples, we show three response theories that follow this pattern in Fig. 2. Figure 2(a) shows the Fermi surface structure of a 3D time-reversal-invariant Weyl semimetal having a Weyl-node quadrupole moment. The response action of this system is a mixed response between electromagnetic and translation gauge fields, and the inset in the Fermi-surface figure lists which coefficients Q_{ab} are nonvanishing. Some details of this response were discussed in Refs. [17,18,24], the former of which connected the response to rank-2 chiral fermions on the surface of the 3D Weyl semimetal. Figure 2(b) shows the Fermi surface structure of a 2D Dirac semimetal having a Dirac-node quadrupole structure. This response represents a momentum current responding to a translation gauge field (e.g., a strain configuration). Its form shares some similarities with the torsional Hall viscosity [11,71,73–75], though a precise connection is left to future work. Finally, in Fig. 2(c), we show the Fermi surface for an unusual nodal line semimetal formed from stacking the Dirac-node quadrupole semimetal in Fig. 2(b). While one might have naively expected two independent Fermi rings, we instead find a new type of Fermi-surface structure where the Fermi lines join at two crossing cap regions to form a cage.

The symbols on the right-hand side in Fig. 2 indicate the connections between these theories: (i) The response of the nodal line structure is just a stacked version of the 2D Dirac-node quadrupole semimetal response from Fig. 2(b), and (ii) one can heuristically consider the four-node Weyl response in Fig. 2(a) to be a dimensional extension of the response in Fig 2(b) via pumping.

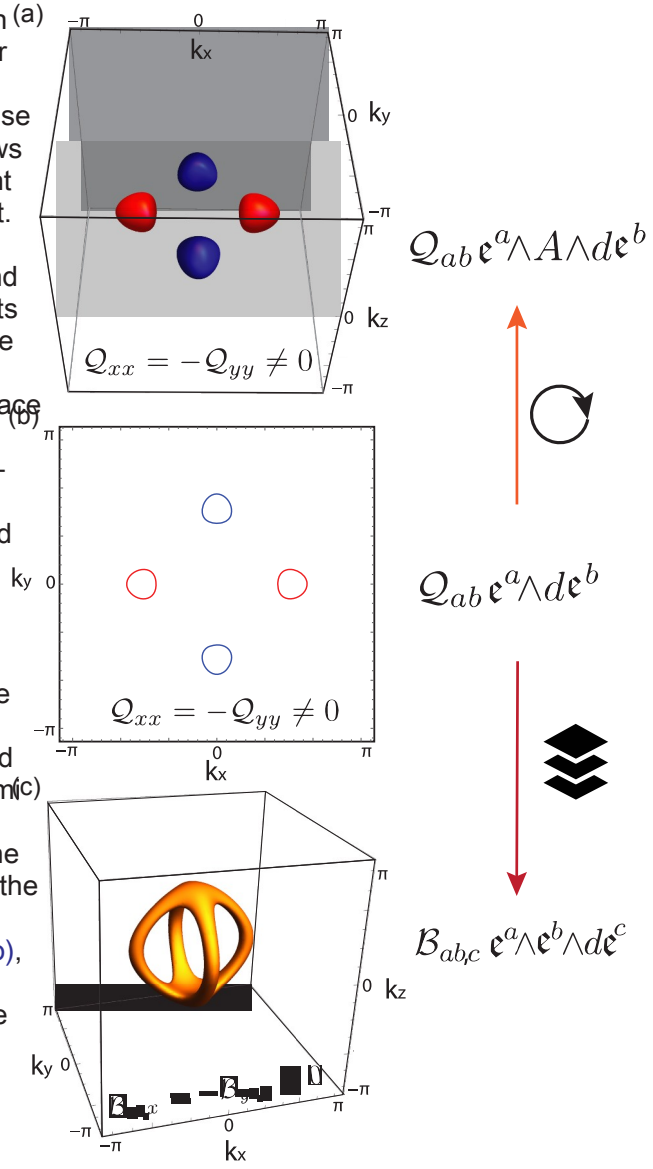

FIG. 2. (a) Fermi surfaces of a 3D time-reversal-invariant Weyl semimetal with a quadrupole Weyl-node configuration. Red and blue colors denote positive and negative Berry curvature, respectively. The associated action has a coefficient matrix Q_{ab} which is symmetric and proportional to the Weyl-node quadrupole moment. For this configuration, the coefficients Q_{xx} and Q_{yy} are nonvanishing. (b) Similar to (a) except it is the Fermi surfaces for a 2D Dirac semimetal having four Dirac nodes in a quadrupole pattern. The action is described by a symmetric matrix of coefficients Q_{ab}. (c) The Fermi surface of an unusual cagelike nodal line semimetal built from stacking the Dirac-node quadrupole semimetal in (b). The action has a set of coefficients $B_{ab,c}$ which is antisymmetric in a and b. Heuristically, the action in (b) can generate the action in (a) by adiabatic pumping or can generate the action in (c) by stacking.

III. EFFECTIVE RESPONSE ACTIONS

Now that we have described the forms of the various response actions of interest, we spend this section determining their coefficients. All of the response actions in Fig. 1(c) that contain only electromagnetic gauge fields represent insulators, and their coefficients have been studied in detail (e.g., see Ref. [5]). The actions containing translation gauge fields can represent insulators or gapless systems, and the two can often be distinguished by the values of the coefficients. That is, for insulators we expect the coefficients to be quantized in some units (in even spatial dimensions, they are quantized in the presence of some symmetry), while for topological semimetals we expect the coefficients to be a tunable function of the momentum and energy locations of the nodal points or lines. Interestingly, some of the response coefficients for metals and semimetals can take the same values allowed for an insulator, although this would typically require fine-tuning, or extra symmetry. For example, a 1D system can have compensating particle and hole Fermi surfaces such that the total filling is an integer, as one would find in an insulator, yet the system is still gapless. In such a case, we show that the system has additional response terms that have coefficients that are incompatible with a gapped insulator.

Our focus will be on 2D Dirac, 3D Weyl, and 3D nodal line semimetals, and, before we begin our derivations, it is important to acknowledge a key qualitative difference between these types of topological semimetals. Namely, we recall that 2D topological Dirac semimetals and 3D nodal line semimetals require additional symmetry beyond translation symmetry, e.g., composite T I symmetry or a mirror symmetry, to guarantee the local stability of the gapless points or lines in momentum space. This is inherently different from the case of Weyl semimetals in 3D, for which Weyl nodes require only translation symmetry for protection against perturbations. Indeed, a Weyl node can be gapped out only by bringing another Weyl node of opposite chirality to the same point in the Brillouin zone. A similar story applies to (semi)metallic systems in 1D: Each gapless point has a well-defined chirality defined as the sign of the Fermi velocity, and a gap can be opened only after overlapping Fermi points of opposite chiralities.

This distinction in symmetry protection is important for the response theories describing Dirac and Weyl semimetals, as it reflects the well-known structure of anomalies in even and odd spatial dimensions. Furthermore, it impacts our strategy for deriving the response coefficients for these systems. As an example, the response properties of 2D Dirac semimetals can be determined straightforwardly from the Kubo formula if we first apply a symmetry-breaking perturbation that weakly gaps out the nodes and regulates any possible infrared divergences. The resulting insulator response can then be taken to the semimetallic limit if we tune the perturbation to zero. Hence, the effective response action for such systems can be obtained by treating the system as an insulator and applying the Kubo formula or, more generally, a gradient expansion procedure. This method can be applied to 2D and 4D Dirac semimetals and, consequently, 3D nodal line semimetals, since they are just stacks of 2D Dirac semimetals. For such semimetals, we actually have a choice of what symmetry to break, e.g., inversion or time reversal. Which one we need to break depends on the nodal configuration and the action we are intending to generate. For example, in the case of a 2D Dirac semimetal with a pair of nodes, breaking time reversal is well studied and generates a quantum Hall response via a Chern-Simons term. However, breaking inversion symmetry is relatively less studied and generates a mixed Chern-Simons response between an electromagnetic gauge field and a translational gauge field. This is corroborated by the fact that the electromagnetic Chern-Simons action breaks time reversal, while the mixed Chern-Simons term with these fields breaks inversion. We show that the mixed Chern-Simons term has a well-defined limit as the gap closes and inversion symmetry is restored, which leads to a nontrivial response action for the 2D Dirac semimetal.

Alternatively, the response of isolated chiral gapless points in 1D and 3D can be determined if they are viewed as theories that live on the boundary of a higher-dimensional topological insulator or topological semimetal. In the presence of gauge fields, the higher-dimensional bulk generates a current inflow to the boundary to compensate the anomalous response of the gapless boundary modes. From this perspective, we expect that the effective response action of Weyl semimetals in odd spatial dimensions can be obtained by taking the boundary contribution of a higher-dimensional system. The purpose of this approach is the same as applying symmetry-breaking perturbations in even spatial dimensions: to regulate possible infrared divergences. However, chiral semimetals in odd spatial dimensions cannot be gapped out unless translation symmetry is broken. Translation symmetry plays a central role in this work, so we must take this alternative approach in odd spatial dimensions. There are likely other methods that could be applied to derive these response actions in their intrinsic spatial dimension, e.g., via the subtle introduction of an auxiliary θ field, but we choose our procedure since it reinforces the dimensional relationships discussed in the previous section and requires fewer formal tools.

Thus, our strategy for deriving the general form of the coefficients of mixed crystalline-electromagnetic responses is to begin by deriving effective response actions in even spatial dimensions, i.e., 2D and 4D. We do so by identifying gradient expansion contributions (see Appendix B for a brief review) that contain an appropriate effective action constructed out of translational (e^λ) and electromagnetic (A) gauge fields. Then, the response of semimetals in odd spatial dimensions can be obtained by looking at the boundary of a response theory defined in one dimension higher.

A. Effective responses of 2D semimetals

In this subsection, we derive the coefficients of two 2D response actions that contain translation gauge fields, namely, response action (v) from Fig. 1(c) and the response action in Fig. 2(b). We find that the coefficients of these actions are characterized by the dipole and quadrupole moments of the Berry curvature in the 2D Brillouin zone, respectively. When we specialize to 2D Dirac semimetals, the distribution of Berry curvature is sharply localized as π fluxes at the Dirac nodes. Hence, the coefficients become proportional to the dipole and quadrupole moment of the distribution of Dirac nodes.

1. Dirac-node dipole semimetal

Let us start by considering a gapped T -invariant system having broken I symmetry. Under these conditions, the electromagnetic Chern-Simons term, which represents the Hall conductivity, vanishes, and we can consider the mixed linear response of a momentum current responding to an electromagnetic field, or vice versa. Using the Kubo formula, or applying the gradient expansion procedure described in Appendix B, we find the contribution to the

effective action (when the chemical potential lies in the insulating gap) (see also Ref. [62]):

$$S_{e;A} = -e \int d^3r \epsilon^{\alpha}_{\mu} \partial_\nu A_\rho \int \frac{d\omega d^2k}{(2\pi)^3} k_\alpha \Omega^{(3)}_{\mu\nu\rho}(\omega; k); \quad (4)$$

where

$$\Omega^{(3)}_{\mu\nu\rho}(\omega; k) = \mathrm{tr} G_0 \frac{\partial G_0^{-1}}{\partial k_\mu} \frac{\partial G_0}{\partial k_\nu} \frac{\partial G_0^{-1}}{\partial k_\rho} \quad (5)$$

and $G_0(k_\mu)$ is the single-particle Green function. To extract the coefficient of the $\epsilon \wedge dA$ term, we contract $\Omega^{(3)}_{\mu\nu\rho}$ with the totally antisymmetric tensor $(1/3!)\epsilon^{\mu\nu\rho}$. This gives the coefficient

$$c_\alpha = e \frac{\epsilon^{\mu\nu\rho}}{3!} \int \frac{d\omega d^2k}{(2\pi)^3} k_\alpha \Omega^{(3)}_{\mu\nu\rho}(\omega; k) \quad (6)$$

of the response action

$$S_{e;A} = c_\alpha \int e^\alpha \wedge dA. \quad (7)$$

We note that Eq. (6) is very similar to the response coefficient of the standard electromagnetic Chern-Simons term apart from the factor of k_α in the integrand. As such, assuming $\alpha = x, y$, we can use a well-established result to evaluate the frequency integral to obtain [76]

$$\frac{\epsilon^{\mu\nu\rho}}{24\pi^2} \int d\omega d^2k \Omega^{(3)}_{\mu\nu\rho}(\omega; k) = \frac{1}{2\pi} \int_{BZ} d^2k F^{xy}(k); \quad (8)$$

where F^{xy} is the Berry curvature. Hence, we can rewrite c_α as an integral over the BZ by substituting this relationship into Eq. (6) to find

$$c_\alpha = \frac{e}{(2\pi)^2} \int_{BZ} d^2k k_\alpha F^{xy}(k). \quad (9)$$

We have, thus, arrived at the result that c_α is proportional to the αth component of the dipole moment of the distribution of Berry curvature. This coefficient can be nonzero, since it is allowed by broken I and preserved T, i.e., $F^{xy}(k) = -F^{xy}(-k)$. We also note that c_α is independent of the choice of zone center, and shifts of k in the integrand, in general, because the Chern number (Hall conductivity) vanishes in the presence of T.

In a gapped T-invariant system, restoring I symmetry forces c_α to vanish, since $F^{xy}(k) = 0$. However, in gapless systems, this need not be the case. To see this, we apply our result from Eq. (9) to a 2D Dirac semimetal by first introducing a weak perturbation V, which breaks I and opens up a small gap, and then taking the limit $V \to 0$, in which inversion symmetry is restored. In the gapped system, the Berry curvature F^{xy} is distributed smoothly across the entire 2D BZ.

In the gapless limit, however, the Berry curvature distribution develops sharp peaks of weight π localized at the positions of the Dirac points:

$$F^{xy}(k) = \pi \sum_{a=1}^{N_D} \chi_a \delta(k - k^a); \quad (10)$$

where a runs over all Dirac nodes at momenta k^a and $\chi_a = 1$ is an integer indicating the sign of the π-Berry phase around the Fermi surface of the ath Dirac point at a small chemical potential above the node [34]. Ultimately, we find the effective response action of a Dirac-node dipole semimetal is given by

$$S_{DD} = \frac{eP_\alpha}{4\pi} \int e^\alpha \wedge dA; \quad (11)$$

where

$$P_\alpha = \sum_{a=1}^{N_D} \chi_a k^a_\alpha \quad (12)$$

is the dipole moment of the Dirac nodes.

Note that if the Dirac nodes meet at the zone boundary, they can be generically gapped even in the presence of T I symmetry. The resulting insulating phase represents a weak TI having $P_\alpha = G_\alpha$, where G_α are the components of a reciprocal lattice vector. In this case, the action in Eq. (11) describes a stack (i.e., a family of lattice lines or planes corresponding to G_α) of 1D polarized TI chains aligned perpendicular to G_α. To see this explicitly, take $G_x = (2\pi/a_x)\hat{x}$ and set $e^\alpha = \delta^\alpha_\beta$ in Eq. (11) to obtain the action

$$\frac{e}{2} \int \frac{dx}{a_x} \int dt dy E_y = N_x \frac{e}{2} \int dt dy E_y; \quad (13)$$

where N_x is the number of unit cells in the x direction. This action is just N_x copies of the usual θ-term action for 1D, electrically polarized topological insulators ($\theta = \pi$) parallel to the y direction, stacked along $\hat{x}$.

We have now derived Eq. (11) as a quasitopological contribution to the response of a 2D Dirac semimetal where the nodes have a dipolar configuration. However, there is another important subtlety that we now point out. Earlier work has shown that the electromagnetic response of 2D Dirac semimetals with both T and I symmetry is an electric polarization proportional to the Dirac-node dipole moment [34]. Even more recently, connections have been made between mixed translation-electromagnetic responses and the electric polarization [64]. Since we have a clear derivation of the response term, we can use our results to understand the precise connection between the electric

polarization and the coefficient c_α of the $e^\alpha \wedge dA$ response action. Using the standard approach of Ref. [26], the polarization in 2D is

$$P_e^\alpha = \frac{e}{(2\pi)^2} i \int_{BZ} d^2k \langle u_k | \partial_{k_\alpha} u_k \rangle; \quad (14)$$

where $A^\alpha(k) = i\langle u_k | \partial_{k_\alpha} u_k \rangle$ is the Berry connection. Hence, we find that the electric polarization P_e^α is related to c_α by an integration by parts (see Appendix C):

$$P_e^\alpha = \frac{e}{(2\pi)^2} \epsilon^{\alpha\beta} \int d^2k k_\beta F^{xy} + \frac{e}{2\pi} W^\alpha = \epsilon^{\alpha\beta} c_\beta + \frac{e}{2\pi} W^\alpha; \quad (15)$$

where we set the lattice constants equal to unity and the Wilson loop

$$W^\alpha = \oint dk_\alpha A^\alpha(k_\alpha; k_\beta = \pi) \quad (16)$$

is an integral of the Berry connection A^α along the αth momentum direction at a fixed, inversion-invariant transverse momentum $k_\beta = \pi$ at the boundary of the BZ.

From this explicit relationship, we can immediately draw some conclusions. First, in the Dirac semimetal limit, we reproduce the result of Ref. [34] where the polarization is proportional to the Dirac-node dipole moment: $P_e^\alpha = \frac{1}{2} e/(2\pi) \epsilon^{\alpha\beta} p_\beta$. And second, if we have broken inversion symmetry (while T is still preserved), we see that the polarization and the coefficients c_α are not quantized and not equal to each other. This scenario can be found in inversion-breaking insulators with a Berry curvature dipole moment. These insulators have a charge polarization, and they also have a mixed translation-electromagnetic response. However, we find from this calculation, and explicit numerical checks, that they are generically inequivalent. Ultimately, this boils down to the fact that the Wilson loop at the boundary of the BZ requires a symmetry to be quantized, e.g., mirror or inversion. Otherwise, the Wilson loop gives a contribution that distinguishes the polarization and the mixed crystalline-electromagnetic responses. We leave a detailed discussion of this subtle distinction to future work.

In summary, Eq. (11) captures the generic mixed crystalline-electromagnetic response of the bulk of a 2D system with T symmetry. In the limit of a Dirac semimetal, the coefficient of the response coincides with the electric polarization of the system. We note that in this limit there are other nonvanishing response terms, since the system is gapless, but Eq. (11) represents a distinct contribution to the total response of the system to electromagnetic and translation gauge fields. We study an explicit model with this response term in Sec. IV A.

2. Dirac-node quadrupole semimetal

Now we move on to discuss the response of quadrupole arrangements of 2D Dirac nodes as in Fig. 2(b). If the Chern number and momentum dipole moment p_α vanish, then our semimetal has a well-defined momentum quadrupole moment, which is independent of the choice of zone center. We now show that such systems are described by the response action:

$$S_{DQ} = \frac{\hbar Q_{\alpha\beta}}{8\pi} \int e^\alpha \wedge de^\beta. \quad (17)$$

From the derivation in the previous section, we anticipate that, in the limit of a Dirac semimetal band structure, the coefficient $Q_{\alpha\beta}$ of this response action is related to the momentum quadrupole moment of the Dirac nodes. To confirm this statement, let us consider the linear response of a momentum current to a translation gauge field for a gapped system. From the Kubo formula, or gradient expansion, we find a coefficient of the $e^\alpha \wedge de^\beta$ term:

$$Q_{\alpha\beta} \equiv \frac{1}{2} \frac{\epsilon_{\mu\nu\rho}}{3!} \int \frac{d\omega d^2k}{(2\pi)^3} k_\alpha k_\beta \Omega^{(3)}_{\mu\nu\rho}(\omega; k). \quad (18)$$

We can use the relationship mentioned in Eq. (8) to carry out the frequency integral to obtain the coefficient of Eq. (17):

$$Q_{\alpha\beta} = \frac{1}{\pi} \int_{BZ} d^2k k_\alpha k_\beta F^{xy}(k). \quad (19)$$

To apply this to the Dirac-node quadrupole semimetal shown in Fig. 2(b), we evaluate the response by first introducing a symmetry-breaking mass term and then studying the topological response of the resulting gapped system. In this case, the mass term breaks T but has a vanishing total Chern number. In the example at hand, this can be done by adding a k-independent term that opens a local mass of the same sign for each of the four Dirac points in Fig. 2(b). Such a mass term preserves T, which in the gapped system automatically guarantees a vanishing dipole moment of the Berry curvature. This, together with the vanishing Chern number, is necessary so that the momentum quadrupole moment is well defined, independent of the choice of zone center. For this scenario, in the limit that the perturbative mass goes to zero,

$$Q_{\alpha\beta} = \sum_{a=1}^{N_D} \chi_a k_\alpha^a k_\beta^a; \quad (20)$$

which is the Dirac-node quadrupole moment. In Sec. IV B, we explicitly study a model with this Berry curvature configuration and a resulting nonvanishing $Q_{\alpha\beta}$. We see

that, while the Dirac-node dipole moment captures the electric polarization (see Appendix C), the nodal quadrupole moment captures a kind of momentum polarization (see Appendix D) (this time, without the subtlety of the additional Wilson loop contribution discussed above). For comparison, the surface charge theorem relates the bulk electric polarization to a boundary charge, and for the momentum polarization there is a boundary momentum.

B. Effective responses of 1D (semi)metals

Now that we have derived the responses of 2D systems coupled to electromagnetic and translation gauge fields, we use Figs. 1(b) and 2 as guides to generate related responses in 1D and 3D. To get 1D responses, we consider the boundary response of the 2D systems (this subsection), and we stack the 2D responses to get 3D responses of nodal line semimetals (next subsection). We note that in the following discussion we treat translation as a continuous symmetry (as in Appendix A, as this perspective is useful for obtaining the correct response actions from our diagram calculations). One can see Ref. [18], for example, for a discussion that treats the subtleties associated to having a discrete translation symmetry.

It is well known that chiral modes in 1D are anomalous; i.e., charge is not conserved when we apply an electric field. In 1D lattice models, this anomaly is resolved because of fermion doubling; i.e., for every right-moving chiral mode, there is a corresponding left-moving mode that compensates the anomaly. While it is true that the electromagnetic charge anomaly is resolved with such a lattice dispersion, the doubled system can still be anomalous in a different but related sense if we have translation symmetry (see Ref. [18] for a similar discussion).

To be specific, in the presence of translation symmetry, we can consider the momentum current in Eq. (3): $J^\mu_x = \hbar k_x j^\mu$, where j^μ is the particle number current. At low energies, current-carrying excitations lie in the vicinity of Fermi points $k_x^{F;\alpha}$ and carry corresponding particle currents $j^\mu_{\delta\alpha}$. The total contribution to momentum current from these low-lying modes is

$$J^\mu_x = \sum_\alpha \hbar k_x^{F;\alpha} j^\mu_{\delta\alpha}. \tag{21}$$

In the simplest case of a nearest-neighbor lattice model having a single, partially filled band, we have two Fermi points: $k^F \equiv k_x^{F;R} = -k_x^{F;L}$, with $j^\mu_R = \delta\rho_R(-v_F\rho_R)$ and $j^\mu_L = \delta\rho_L(-v_F\rho_L)$, where ρ is the number density. Interestingly, the momentum current in this scenario is

$$J^\mu_x = \hbar k^F(j^\mu_R - j^\mu_L); \tag{22}$$

which, up to a factor of $\hbar k^F$, is just the axial current.

Importantly, even though this lattice model does not have an electromagnetic charge anomaly, $\partial_\mu(ej^\mu_L + ej^\mu_R) = 0$, it does have an axial anomaly:

$$\partial_\mu(j^\mu_R - j^\mu_L) = \frac{eE^x}{\pi\hbar}. \tag{23}$$

Taking this point of view, we can reformulate the axial anomaly in this system as a mixed crystalline-electromagnetic anomaly where an electric field E^x violates conservation of the k_x momentum current:

$$\partial_\mu J^\mu_x = \frac{e\hbar k^F}{\pi\hbar}E^x. \tag{24}$$

More generally, the anomaly is proportional to the momentum dipole moment of the Fermi points, which replaces a factor of $2k_F$ in Eq. (24) (see Appendix E).

There is a conjugate effect that occurs in an applied strain field, which can be implemented as a translation electric field $E^x_x = \partial_x e^x_0 - \partial_t e^x_x$. Naively, such a nonvanishing field generates violations to the conservation law for the usual electromagnetic current according to

$$\partial_\mu(ej^\mu) = \frac{ek^F}{\pi}E^x_x \tag{25}$$

(again, see Appendix E for a more general expression in terms of the momentum dipole). However, this equation is not quite correct if we have an isolated system with a fixed number of electrons, and, hence, we must be careful when considering time-dependent changes to e^x_x as we now describe.

To gain some intuition for Eq. (25), consider increasing the system size by one lattice constant a during a time T by adding an extra site to the system: $\int_R dx dt E^x_x = a$ (one can also think of threading a dislocation into the hole of a 1D periodic system). From the anomaly equation, we would find that the amount of charge in the system changes by ek^Fa/π, as one would expect for adding a unit cell to a translationally invariant system having a uniform charge density $\rho = ek^F/\pi$. However, there is a subtlety that we can illustrate by considering a system having a fixed number of electrons $N_e = k^F L_x/\pi$, which we strain by uniformly increasing the lattice constant. Assuming a uniform system, the anomalous conservation law in this case becomes

$$\partial_t\rho = \partial_t\left(\frac{ek^F}{\pi}e^x_x\right). \tag{26}$$

Crucially, we note that if we increase the system size with fixed particle number, then k^F decreases. Indeed, in the small deformation limit, the momenta are proportional to $(e^x_x)^{-1}$, since their finite size quantization depends

inversely on the system size. Using this result, the conservation law becomes

$$\partial_t \rho = \frac{e}{\pi}\left(\partial_t e^x_x k^F + k^F \partial_t e^x_x\right) = \frac{e k^F}{\pi}\left(-\partial_t e^x_x + \partial_t e^x_x\right) = 0;$$

where we use $\partial_t\left(e^x_x\right)^{-1} = -\left(e^x_x\right)^{-2}\partial_t e^x_x$.

The outcome that $\partial_t \rho = 0$ is the result one would expect by stretching the system uniformly while keeping the number of particles fixed. To clarify, at a fixed particle number we know the total charge cannot change; however, it perhaps seems counterintuitive that the density does not decrease if we stretch the system. The reason is that the quantity ρ above, which is defined as $\delta S/\delta A_0$, is not a scalar density. Indeed, for general geometries, the scalar charge density would be defined as

$$\bar{\rho} = \frac{1}{e^x_x}\frac{\delta S}{\delta A_0}; \tag{27}$$

where the e^x_x is essentially playing the role of the determinant of a spatial metric. To calculate the total charge, we would then use

$$Q = \int dx e^x_x \bar{\rho} = \int dx \rho: \tag{28}$$

Indeed, the scalar charge density $\bar{\rho}$ still decreases as the system is stretched, since $\partial_t \bar{\rho} \propto \partial_t P_x$ which decreases as the system size increases for fixed electron number.

The effective response action of the 1D system can be derived as a boundary effective action of an appropriate 2D theory. In fact, we have already seen such a 2D system when studying the 2D Dirac semimetal with Dirac nodes arranged in a dipolar fashion. The bulk response for this 2D system with a weak inversion-breaking gap is Eq. (11). As mentioned above, this bulk theory implies that the system has an electric polarization. From the surface-charge theorem for polarization, we expect that the boundary will have a charge density equal the polarization component normal to the boundary. The contribution to the boundary effective action from Eq. (11) is

$$S_\partial = \frac{e}{4\pi}\int P_\alpha \, e^\alpha \wedge A:$$

From this, we can extract the boundary charge density: $\rho_\partial = (e/2\pi)(P_\partial/e^\partial_\partial)$, where P_∂ is the component along the boundary and e^∂_∂ is the diagonal translation gauge field component along the boundary that is simply equal to unity in nondeformed geometries.

While the form of this action is what we expect for a 1D metal, the coefficient is half the size it should be. The reason is that, on the edge of the 2D Dirac semimetal, the momentum-space projections of the bulk Dirac nodes in the edge BZ represent points where the edge filling changes by $e/2$ [34], not e as would be the case for a 1D Fermi point in a metal. Hence, for a metal, we expect a result twice as large (we see a similar result in Sec. III E when comparing the boundary response of a 4D system to that of a 3D Weyl semimetal). Thus, the action for the 1D system is

$$S_{1D;D} = \frac{e}{2\pi}\int P_\alpha \, e^\alpha \wedge A: \tag{29}$$

From this form, we can identify $P = (-\Delta\mu/\hbar, \Delta k_x)$ such that $P_x/2\pi$ is simply the filling fraction of the 1D metal and $P_t/2\pi$ measures the imbalance of left- and right-moving excitations in the system ($\Delta\mu = \mu_R - \mu_L$).

Introducing a charge current vector

$$j^\mu = \frac{e}{2\pi}\epsilon^{\mu\nu}P_\nu = \frac{e}{2\pi}(\Delta k_x, -\Delta\mu/\hbar); \tag{30}$$

we can recast Eq. (30) in the most familiar form: $S_{1D;D} = \int dt dx j^\mu A_\mu$. Thus, we have now generated the action (ii) from Fig. 1(c). Let us also note that the edge states of the Dirac semimetal can be flat, while the 1D context we mentioned above has a dispersion. However, the key feature of both cases is that as momentum is swept across the 1D BZ (1D surface BZ for the 2D case) the filling of the states changes in discrete jumps at either the Fermi points in 1D or the (surface-projected) Dirac points in 2D. It is this change in the filling that is captured by the quantity P_x and does not depend on the dispersion in a crucial way.

Now that we have this example in mind, we can ask what the analogous 1D boundary system is for the Berry curvature quadrupole action Eq. (17). We mention that this bulk response represents a momentum polarization, which implies that the boundary should have a momentum density parallel to the edge. Indeed, we expect that such a 1D system will have a vanishing Fermi-point dipole moment (i.e., the filling is integer) but a quadrupole moment that is nonvanishing [see Fig. 3(b)].

From the point of view of the translation gauge fields, such band structures are chiral, since either the right movers or left movers carry larger momentum charge. To see this, consider a 1D Fermi surface with right movers at momenta K_F and left movers at momenta Q_F. Let us further restrict our attention to currents for which the net number of right movers (and of left movers) is zero, e.g., $\rho_R(K_F) + \rho_R(-K_F) = 0$. Defining $\delta\rho_R = \frac{1}{2}\rho_R(K_F) - \rho_R(-K_F)$ and $\delta\rho_L = \frac{1}{2}\rho_L(Q_F) - \rho_L(-Q_F)$, we see that the momentum gauge field couples to

$$J^\mu_x = K_F\delta\rho_R + Q_F\delta\rho_L: \tag{31}$$

Thus, we see that, for $K_F \neq Q_F$ [as in Fig. 3(b)], the momentum gauge field couples differently to right- and left- moving density fluctuations. In the extreme limit that $Q_F = 0$, the momentum gauge theory is fully chiral.

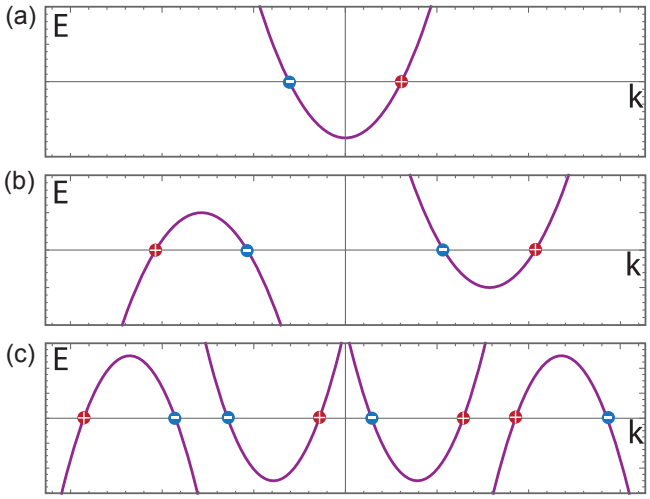

FIG. 3. (a) One-dimensional band structure of an ordinary metal. The pair of gapless points is marked by the sign of their respective chiralities, highlighting the momentum-space dipole characterizing the response of the system. (b) Band structure of a 1D metal characterized by a momentum quadrupole moment. The system has an integer (vanishing in this case) charge filling but a nonzero momentum. (c) Band structure of a 1D metal characterized by a momentum octupole moment. The system has an integer (vanishing) filling, a vanishing momentum, but a nonvanishing expectation value for the square of the momentum. See Appendix E.

More generally, in a 1D system with a Fermi-point quadrupole [cf. Eq. (20)] $Q_{xx} = \sum_{a=1}^{N_F} \chi_a (k_a - k_0)^2$ and fixed electric charge, this chiral coupling leads to an anomaly in the presence of a nonvanishing translation gauge field:

$$\partial_\mu J^\mu_x = \frac{\hbar Q_{xx}}{4\pi} E_x. \quad (32)$$

This anomaly implies that if we turn on a translation gauge field (e.g., via strain), then we will generate momentum as shown in Appendix E [77].

The response theory describing such a 1D system is similar to that describing the chiral boundary of a Chern-Simons theory. Indeed, if we start from Eq. (17) and derive the boundary response (and compensate for a similar factor of 2 as mentioned above in the momentum-dipole case), we arrive at an effective action:

$$S = -\frac{\hbar}{4\pi} \int d^2r (Q_{xx} e^x_x e^x_t + Q_{xt} e^x_x e^t_t). \quad (33)$$

In this effective action, the momentum quadrupole moment of the Fermi points Q_{xx} encodes the ground state momentum density (see Appendix E). The quantity Q_{xt} is the mixed Fermi-point quadrupole moment in momentum and energy, but we leave a detailed discussion of such mixed moments to future work.

The arguments of this section can be extended to look at higher moments of the chirality-weighted Fermi momenta, which are proportional to the ground state expectation values of higher and higher powers of momenta. To describe these properties and related response phenomena, we can introduce gauge fields $e^{abc\ldots}$ that couple to higher monomials of momentum, $k_a k_b k_c \ldots$. For example, the fields that couple to zero powers or one power of momentum are the electromagnetic A and translation gauge fields $k_x e^x$, respectively, and we could introduce a coupling $k_a k_b e^{ab}$ to the set of 1-form gauge fields e^{ab}, e.g., $k_x^2 e^{xx}$. We describe the hierarchical anomalies associated to these gauge fields in Appendix E.

C. Effective responses of 3D nodal line semimetals

We can now use our 2D results from Sec. III A to generate the responses of two types of nodal line semimetals in 3D. To generate the two types we imagine stacking either the action in Eq. (11) or the action in Eq. (17). The action resulting from the former has been discussed in Refs. [19,35]; the second is, to the best of our knowledge, new. From our arguments for gapped systems in Sec. II, we expect that the form of the actions we obtain from stacking will contain an extra wedge product with the translation gauge field in the stacking direction. To be explicit, suppose we are stacking up 2D semimetals (that are parallel to the xy plane) into the z direction. By stacking decoupled planes of the responses in either Eq. (11) or (17), we expect to find

$$S = \frac{eP_\alpha}{4\pi a_z} \int e^z \wedge e^\alpha \wedge dA$$

or

$$S = \frac{\hbar Q_{\alpha\beta}}{8\pi a_z} \int e^z \wedge e^\alpha \wedge de^\beta;$$

respectively, where $\alpha, \beta = x, y$. The forms of these actions match action (viii) in Fig. 1(c) and the action in Fig. 2(c), respectively. We note that the stacked, decoupled systems simply inherit the response coefficient of the 2D system.

We want to consider more general configurations of systems with stacked and coupled planes, perhaps stacked in several directions. As we have seen, if the layers we stack are decoupled, then each layer contributes the same amount. This contribution (for a stack in the z direction) is captured by the integral $1/a_z \int e^z = N_z$, where N_z is the number of layers. However, if the layers are coupled, then each fixed-k_z plane can have a different amount of Dirac-node dipole $[P_\alpha(k_z)]$ or Dirac-node quadrupole moment $[Q_{\alpha\beta}(k_z)]$, respectively. The total coefficient is then determined by the sum over all values of k_z. One can also have

stacks in any direction, not just the z direction. Hence, in this more generic scenario, the actions become

$$S_{DD3} = eB_{\alpha\beta} \int e^{\alpha} \wedge e^{\beta} \wedge dA \tag{34}$$

and

$$S_{DQ3} = \hbar B_{\alpha\beta;\gamma} \int e^{\alpha} \wedge e^{\beta} \wedge de^{\gamma}; \tag{35}$$

with coefficients

$$B_{\alpha\beta} = \frac{1}{4(2\pi)^2} \epsilon^{\alpha\beta\sigma} \int d^3k k_{\delta} F^{\sigma\delta} \tag{36}$$

and

$$B_{\alpha\beta;\gamma} = \frac{1}{6(2\pi)^2} \epsilon^{\alpha\beta\sigma} \int d^3k k_{\gamma} k_{\delta} F^{\sigma\delta}; \tag{37}$$

where $F^{\mu\nu}$ is the Berry curvature of the $k_\mu k_\nu$ plane. These forms of the coefficients capture scenarios with more complicated nodal line geometries. Indeed, as previously shown in Ref. [35], the coefficient $B_{\alpha\beta}$ is determined by the line nodes that have nonvanishing area when projected into the αβ plane. Additionally, for nodal line semimetals with T I symmetry, the coefficient is proportional to the charge polarization in the direction normal to the αβ plane [35]. We can see this explicitly by integrating Eq. (36) by parts with the same caveats mentioned in Sec. III A 1 surrounding Eq. (15).

Analogously, the coefficient $B_{\alpha\beta;\gamma}$ can represent a kind of "momentum" polarization where the polarization is again normal to the αβ plane and the charge that is polarized is the momentum along the γ direction. We can see this heuristically by integrating by parts using the derivatives in the $F^{\sigma\delta}$ to find

$$B_{\alpha\beta;\gamma} \sim -\frac{1}{2(2\pi)^2} \int d^3k (\delta^{\alpha\beta\sigma} k_{\gamma} A^{\sigma} - \epsilon^{\alpha\beta\gamma} k_i A^i); \tag{38}$$

where we use the ~ symbol to indicate that there are boundary terms we have dropped that can be important if the line nodes span the Brillouin zone. We can see from this form that the coefficient for the case when α, β, and γ are not all different, e.g., $B_{xz;x}$, is proportional to the polarization in the y direction (i.e., normal to the xz plane) weighted by the momentum in the x direction.

We note that, for $B_{\alpha\beta}$ to be well defined, the Chern number in each plane must vanish. In addition to this constraint, $B_{\alpha\beta} = 0$ is a necessary constraint for $B_{\alpha\beta;\gamma}$ to be well defined. These hierarchical requirements are analogous to the usual requirements for the ordinary (magnetic) dipole and (magnetic) quadrupole moments of the electromagnetic field to be independent of the choice of origin. Here, the role of the magnetic field distribution is being played by $F^{\rho\sigma}(k)$, and, for example, the constraint on the vanishing Chern number eliminates the possibility of magnetic monopoles (i.e., Weyl points).

D. Effective responses of 4D semimetals

Our next goal is to determine the coefficients for the response actions of 3D Weyl point-node semimetals. However, because the Weyl nodes in 3D exhibit an anomaly, the responses are subtle to calculate intrinsically in 3D. Instead, to accomplish our goal, we first carry out more straightforward calculations of the responses of 4D semimetals and then return to 3D either by considering the boundary of a 4D system or by compactifying and shrinking one dimension of the bulk. Hence, as a step toward 3D semimetals, in this subsection, we provide the derivation for effective response actions of semimetals in 4D.

The first action we consider is of the form

$$S = c_{\alpha} \int e^{\alpha} \wedge dA \wedge dA; \tag{39}$$

where for our purposes $\alpha = x, y, z, w$. Collecting all terms in the gradient expansion that have this field content, we obtain

$$S = \frac{e^2}{\hbar} \int d^5x \epsilon^{\alpha}_{\mu\nu\rho\sigma\tau} \partial_{\nu} A_{\rho} \partial_{\sigma} A_{\tau} \times \int \frac{d\omega d^4k}{(2\pi)^5} k_{\alpha} \Omega^{(5)}_{\mu\nu\rho\sigma\tau}(\omega; k); \tag{40}$$

where

$$\Omega^{(5)}_{\mu\nu\rho\sigma\tau}(\omega; k) = \mathrm{tr} G_0 \frac{\partial G_0^{-1}}{\partial k_{\mu}} \frac{\partial G_0}{\partial k_{\nu}} \frac{\partial G_0^{-1}}{\partial k_{\rho}} \frac{\partial G_0}{\partial k_{\sigma}} \frac{\partial G_0^{-1}}{\partial k_{\tau}}$$

and $G_0(\omega; k)$ is the single-particle Green function. To determine the coefficient c_α, we project this coefficient onto the totally antisymmetric part, and then, just as in Eq. (8), we can carry out the frequency integral [76] to obtain the simpler expression

$$\int \frac{d\omega d^4k}{2\pi} \frac{\epsilon_{\mu\nu\rho\sigma\tau}}{5!} k_{\alpha} \Omega^{(5)}_{\mu\nu\rho\sigma\tau}(\omega; k) = \frac{1}{16} \int_{BZ} d^4k k_{\alpha} \epsilon_{ijkl} F^{ij} F^{kl}. \tag{41}$$

Hence, the response coefficient takes the form

$$c_{\alpha} = \frac{e^2}{\hbar} \frac{1}{16(2\pi)^2} \int_{BZ} d^4k k_{\alpha} \epsilon_{ijkl} F^{ij} F^{kl} = \frac{e^2 P_{\alpha}}{16\pi^2 \hbar}; \tag{42}$$

where we introduce

$$P_\alpha = \frac{1}{16\pi^2}\int_{BZ} d^4k k_\alpha \varepsilon_{ijkl} F^{ij} F^{kl}. \quad (43)$$

As we see from this calculation, similar to 2D, the 4D response theories can be characterized by the distribution of the quantity $\varepsilon_{ijkl} F^{ij} F^{kl}$ across the 4D Brillouin zone. For our focus, let us consider the case where the 4D system is a semimetal with a set of isolated Dirac points (linearly dispersing band touching where four bands meet). Without symmetry, these Dirac points are locally unstable in momentum space to the opening of a gap. If we open up an infinitesimally small energy gap, the quantity $\varepsilon_{ijkl} F^{ij} F^{kl}$ becomes well defined across the entire BZ, and its distribution takes the following form in the massless limit:

$$\varepsilon_{ijkl} F^{ij} F^{kl} = \sum_{a=1}^{N_D} 16\pi^2 \chi_a \delta(k - k_a). \quad (44)$$

If we substitute this into Eq. (43), then we immediately see that P_α becomes the momentum space dipole of the set of 4D Dirac nodes. Let us also comment that, if we integrate Eq. (43) by parts, we see that P_α can also be interpreted as a set of magnetoelectric polarizabilities [5,28]. Just as in the case of the polarization of a 2D Dirac semimetal, the integration by parts generates a boundary term that captures the magnetoelectric polarizability coming from the 3D boundaries of the 4D BZ. Hence, the connection between the total magnetoelectric polarizability and the mixed translation-electromagnetic response is exact only in the symmetric limit when the boundary term is quantized.

In summary, a 4D response of a system characterized by a dipolar distribution of the $\varepsilon_{ijkl} F^{ij} F^{kl}$ quantity reads

$$S = \frac{e^2 P_\alpha}{16\pi^2 \hbar}\int e^\alpha \wedge dA \wedge dA. \quad (45)$$

Similar to 2D, if the dipolar response vanishes, we can obtain a momentum quadrupole response coefficient for the action:

$$S = \frac{eQ_{\alpha\beta}}{16\pi^2}\int e^\alpha \wedge de^\beta \wedge dA; \quad (46)$$

where $Q_{\alpha\beta}$ is a symmetric matrix determined by the momentum space quadrupole moment of the 4D Dirac nodes. Finally, if both the dipolar and quadrupolar responses vanish, we can consider an octupolar distribution that gives the response coefficient for the action:

$$S = \frac{\hbar O_{\alpha\beta\gamma}}{48\pi^2}\int e^\alpha \wedge de^\beta \wedge de^\gamma; \quad (47)$$

where $Q_{\alpha\beta\gamma}$ is determined by the momentum space octupole moment of the 4D Dirac nodes. We leave the discussion of octupolar configurations of Dirac and Weyl nodes to future work. We also mention that, similar to 2D, for these responses to be independent of the choice of BZ origin, we require that the second Chern number of the 4D system vanishes. Alternatively, if the second Chern number is nonvanishing, then the boundary of the system contains a nonvanishing chirality of Weyl nodes. As such, the anomalous charge response of the chiral boundary does not allow us to uniquely determine the momentum response on the boundary.

Before moving on to 3D, let us briefly present some physical intuition about the response in Eq. (45). Consider a 4D time-reversal- and inversion-invariant system having two Dirac nodes separated in the k_z direction. To simplify the discussion, let us also assume the system has mirror symmetry M_z. The assumed symmetries imply that each fixed-k_z volume can be treated as an independent 3D insulator having 3D inversion symmetry, and, hence, the magnetoelectric polarizability of these 3D insulator subspaces is quantized [5,78,79]. Now, if we sweep through k_z, then each bulk 4D Dirac point crossing changes the magnetoelectric polarizability of the fixed-k_z volume by a half integer (i.e., changes the related axion angle by π) [5]. Since the magnetoelectric polarizability jumps between its quantized values as we pass through the two bulk Dirac nodes, the k_z Brillouin zone splits into two intervals: (i) an interval with a vanishing magnetoelectric polarizability and (ii) an interval with a nonvanishing quantized magnetoelectric polarizability. Indeed, we could have anticipated this result from the form of the action Eq. (45) when $\alpha = z$; i.e., the action represents stacks of 3D topological insulators that each have a nonvanishing magnetoelectric polarizability.

E. Effective responses of 3D semimetals

From this discussion, we see that, in the presence of symmetry, the 4D bulk Dirac-node dipole moment determines the magnetoelectric polarizability of these 4D topological semimetals via Eq. (45). We want to connect this result to 3D semimetals in two ways. First, we consider the 3D boundary of the 4D system, and then we consider the spatial compactification of one spatial dimension.

Let us begin by considering the boundary response action from Eq. (45). For the model system described at the end of the previous subsection, we know the system has a k_z-dependent magnetoelectric polarizability. Consider a boundary in the fourth spatial direction w. Since the magnetoelectric polarizability is changing from inside to outside of the boundary, the boundary itself has a nonvanishing Hall conductivity. For our example system, each fixed-k_z slice of this boundary has a Hall conductivity, σ_{xy}, which is quantized but possibly vanishing. Additionally, since the bulk 4D Dirac nodes are separated in the k_z

direction, they project to gapless points in the 3D surface BZ (on surfaces that have at least one direction perpendicular to the z direction) where the Hall conductivity discretely jumps by $\Delta\sigma_{xy} = e^2/2h$.

From this phenomenology, i.e., discrete Hall conductivity jumps as we sweep through k_z, we expect that the boundary response of Eq. (45) captures the same response as a Weyl semimetal that has a nonvanishing momentum space dipole moment of the Weyl nodes in the z direction. Indeed, the generic boundary contribution from Eq. (45) has the form

$$S_{WD} = \frac{e^2 P_\alpha}{8\pi^2\hbar}\int e^\alpha \wedge dA \wedge A; \qquad (48)$$

which was proposed by Ref. [33] to describe the response of Weyl semimetals, though in the more conventional form using an axion field and without the translation gauge field. Here, P_α, $\alpha = x, y, z$ is the momentum dipole of the Weyl nodes in the αth direction. This action is represented as (ix) in Fig. 1(c). We note that the coefficient in Eq. (48) is twice as large as the actual boundary term derived from Eq. (45). This is because, when k_z passes through a single Weyl point, we have $e_{ijk}\Delta\sigma_{jk} = e^2/h$, where the surface the response of the 4D system has jumps of half the size. This is analogous to the fact that a 1D metal has an integer jump in the filling as we pass through a Fermi point, whereas the surface of a 2D Dirac semimetal has a boundary "filling" that jumps by a half integer as we pass through a gapless point in the surface BZ.

We can repeat this analysis for Eq. (46). The coefficient of this term is proportional to the momentum space quadrupole moment of the nodal points. Unfortunately, the phenomenology of this term is not as easy to analyze in 4D, because it is not generated from a lower-dimensional system in a clear way [80]. By analogy with the previous case, the bulk 4D Dirac nodes project to a quadrupole of 3D Weyl nodes on the surface. We can extract the form of the 3D action we want by taking the boundary term generated from Eq. (46). Then, accounting for the factor of 2 as in the previous case, we arrive at

$$S_{WQ} = \frac{eQ_{\alpha\beta}}{8\pi^2}\int e^\alpha \wedge de^\beta \wedge A: \qquad (49)$$

(Note that, since $Q_{\alpha\beta}$ is symmetric, the related contribution of the form $eQ_{\alpha\beta}/8\pi^2 \int e^\alpha \wedge e^\beta \wedge dA$ vanishes.) This action is the same as that shown in Fig. 2(a). It produces a mixed crystalline-electromagnetic response and represents a rank-2 vector charge response when certain mirror symmetries are preserved [17]. Its response coefficient is determined by the momentum space quadrupole moment of the Weyl nodes.

Finally, we come to the action (x) in Fig. 1(c). Let us briefly sketch some salient features of this response, while we leave a detailed discussion to future work. We can arrive at this action using a formal compactification of the action in Eq. (45) [5]. First, we can integrate that action by parts to arrive at

$$\frac{e^2 P_\alpha}{16\pi^2\hbar}\int A \wedge de^\alpha \wedge dA;$$

where we ignore the boundary term. We now want to dimensionally reduce the fourth spatial direction w, which we accomplish by choosing periodic boundary conditions in w and letting the size of the system in this direction shrink toward zero. In this limit, any derivatives with respect to w are (formally in our case) dropped [81]. The resulting nonvanishing contribution is

$$\frac{e^2 P_\alpha}{8\pi^2\hbar}\int dw A_w \int de^\alpha \wedge dA;$$

where the integral and exterior derivative in the second factor are over only the remaining four spacetime dimensions. We can now make the definition

$$\Theta \equiv 2\pi\frac{e}{h}\int dw A_w \qquad (50)$$

to arrive at action (x) from Fig. 1(c):

$$\frac{eP_\alpha}{8\pi^2}\int \Theta de^\alpha \wedge dA: \qquad (51)$$

To illustrate some of the phenomenology of this action, let us assume that $P_z \neq 0$. Additionally, let us assume that we maintain time-reversal and inversion symmetry. As such, $\Theta = 0, \pi$. To begin, we see that the action in Eq. (51) is a total derivative if Θ and P_α are spacetime independent. The resulting pure boundary term is just proportional to the response of a 2D weak TI (or 2D Dirac semimetal), i.e., Eq. (7). Depending on the symmetry of the surface, this implies that we expect the surface to be gapped except for possibly isolated Dirac points. Since the boundary terms appear as $\sim e\wedge dA$, we expect that surfaces normal to $\hat{x}$ ($\hat{y}$) will harbor a y polarization (x polarization); i.e., the polarization is tangent to the surface.

Importantly, the sign of the polarization depends on the interpolation of Θ between its nontrivial bulk value of $\Theta = \pi$ and the trivial vacuum value $\Theta = 0$ outside the system. For neighboring surfaces where the effective sign of the polarization changes, we anticipate hinge charges where surfaces intersect, since the polarizations are converging or diverging from the hinges. Thus, the response of this system is similar to a stack of 2D planes of quadrupole moment having component $q_{xy} \neq 0$. In this scenario, coupled quadrupole planes could lead to either a higher-order weak topological insulator having a quadrupole moment or a higher-order topological semimetal with

boundary (and possibly bulk) Dirac nodes [82,83]. To make further progress, it would be advantageous to have a microscopic derivation of the coefficient in Eq. (51) intrinsically in 3D. Hence, we leave further discussion of this action to future work.

IV. EXPLICIT RESPONSE CALCULATIONS FOR LATTICE MODELS

Now that we have completed the derivations of the actions in Figs. 1(c) and 2, we provide a series of model examples that manifest these responses. Using these models, we can numerically calculate the various charge and momentum responses to electromagnetic and translation gauge fields, providing an independent verification of the coefficients derived in the previous section. Some of the models and responses we discuss below have appeared elsewhere in the literature, while others have not. We carry out this analysis in the same order as the previous section, i.e., point-node Dirac semimetals in 2D, nodal line semimetals in 3D, and then point-node Weyl semimetals in 3D. Calculations for 1D systems are carried out analytically in Sec. III B, and additional discussion can be found in Appendix E.

A. 2D Dirac-node dipole semimetal and insulator

We begin with the time-reversal-invariant 2D systems discussed in Sec. III A that exhibit a mixed crystalline-electromagnetic response. Since T is preserved, the usual Chern-Simons, Hall-effect response of the electromagnetic field vanishes. Instead, the response action derived in Sec. IV A takes the form of a mutual Chern-Simons term [64]:

$$S[A_\mu, e^\lambda_\mu] = \frac{e}{4\pi} P_\lambda \int e^\lambda \wedge dA. \tag{52}$$

Unlike the purely electromagnetic polarization response action considered in Ref. [34], this formulation of the low-energy response theory also includes bulk electromagnetic responses to the translation gauge fields. For example, by taking a functional derivative with respect to A_μ, we have

$$\begin{aligned} \rho &= -\frac{e}{4\pi} P_\lambda \varepsilon^{ij} \partial_i e^\lambda_j; \\ j^x &= \frac{e}{4\pi} P_\lambda (\partial_t e^\lambda_y - \partial_y e^\lambda_t); \\ j^y &= -\frac{e}{4\pi} P_\lambda (\partial_t e^\lambda_x - \partial_x e^\lambda_t). \end{aligned} \tag{53}$$

We see that the first equation predicts an electric charge density localized on a dislocation in the bulk of the lattice, which is exactly the phenomenology we expect for a weak topological insulator [38] or a 2D Dirac semimetal. The action (52) also predicts a bulk momentum response to the electromagnetic field when varied with respect to e^μ:

$$\begin{aligned} J^t_\lambda &= -\frac{e}{4\pi} P_\lambda B_z; \\ J^i_\lambda &= -\frac{e}{4\pi} P_\lambda \varepsilon^{ij} E_j; \end{aligned} \tag{54}$$

where E_i and B_i are the components of electric and magnetic fields, respectively. In the inversion-symmetric limit and in the absence of lattice defects and deformations, for which the crystalline gauge fields reduce to $e^\lambda_\mu = \delta^\lambda_\mu$, Eq. (53) simply reproduces the boundary charge and current responses of an ordinary 2D Dirac semimetal or weak topological insulator, which harbors a nonvanishing electric polarization. However, as we mention in Sec. III A 1 and comment further on below, we do not expect the coefficient of this action to match the electric polarization when inversion is strongly broken.

While the electric polarization and magnetization responses of Dirac semimetals were discussed in detail in Ref. [34], the momentum responses in Eq. (54) and the charge responses to translation fluxes (i.e., dislocations) in Eq. (53) are less familiar. Thus, we explicitly calculate these responses using a minimal tight-binding model. For simplicity, we employ a two-band Bloch Hamiltonian that can model both 2D Dirac semimetals and weak topological insulators:

$$\begin{aligned} H(k) = V_I \sigma^x &+ \sin(k_y a_y)\sigma^y \\ &+ [m - \cos(k_x a_x) - \cos(k_y a_y)]\sigma^z. \end{aligned} \tag{55}$$

When $V_I = 0$, H has both inversion symmetry, $I = \sigma^z$, and (spinless) time-reversal symmetry, $T = K$. In this symmetric regime, m can be chosen to produce a semimetal with Dirac points located at, for example, $(k_x, k_y) = (\pi/2a_x, 0)$, when $m = 1$. In the semimetal phase, turning on $V_I \sigma^x$, which breaks inversion while preserving T, generates a mass term that opens a gap at the Dirac points. The signs of the Berry curvature localized near the two now-gapped Dirac points are opposite, as shown in Fig. 4(a), with the sign at a particular point determined by the sign of the perturbation V_I. Hence, the total Berry curvature of the occupied band integrated over the entire BZ, equivalent to the Chern number, is zero, and, hence, the Berry curvature dipole is well defined.

To confirm our analytic calculations of the response coefficients, we first calculate the momentum density localized around an out-of-plane magnetic flux Φ_z using the tight-binding model Eq. (55). In order to determine the k_x momentum density in the lattice model, we must introduce magnetic flux in a fashion that preserves translation symmetry in the $\hat{x}$ direction. We show the configuration that we employ in Fig. 4(b). This configuration keeps the crystal momentum k_x as a good quantum number and

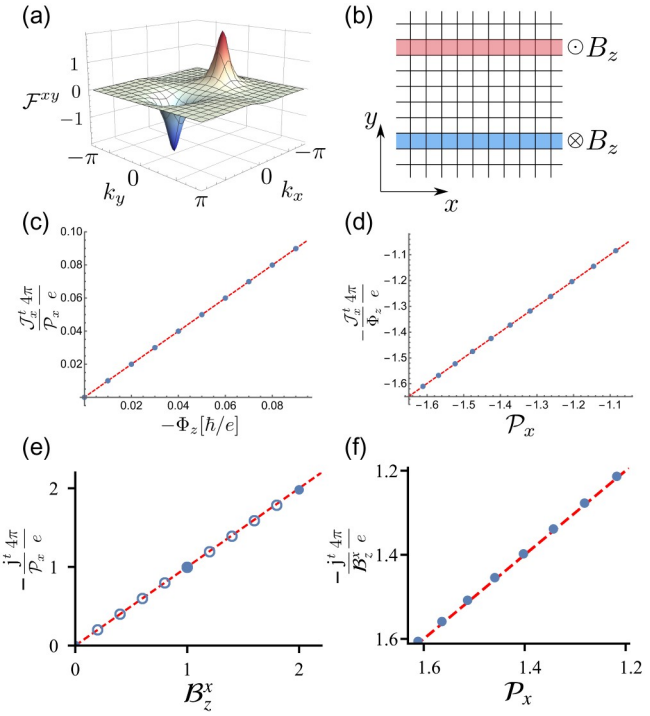

FIG. 4. (a) Plot of the Berry curvature across the 2D Brillouin zone for the Dirac-node dipole semimetal model (55) for $m = 1.1$ with an added inversion-breaking perturbation with $V_l = -0.5$. We use this model to probe the k_x momentum density response. For that, we consider a completely periodic system and insert the magnetic flux Φ_z thorough two lines of plaquettes such that the translational symmetry along the $\hat{x}$ direction is preserved, as shown in (b). (c) shows the k_x momentum density localized around one line of plaquettes penetrated by the magnetic field B_z as a function of magnetic flux. (d) shows the k_x momentum density as a function of Berry curvature dipole moment P_x defined in Eq. (9), which we tune in our model by varying the parameter m between $m = 1.0$ and $m = 1.5$. (e) and (f), we show analogous calculations for the charge density response to a translation flux with Burgers vector in the x direction as a function of (e) translation flux at fixed Berry curvature dipole and (f) Berry curvature dipole at fixed translation flux. The open circles in (e) represent Burgers vector choices that are not integer multiples of a lattice constant. The red dashed lines in (c)–(f) are guides to the eye indicating a slope of 1.

allows us to compute the value of J_x^t as the probability density of the occupied single particle states weighted by their momentum $\hbar k_x$. The results of the numerical calculations are presented in Figs. 4(c) and 4(d), where we study how the excess k_x momentum density bound to magnetic flux behaves as a function of both the magnetic flux Φ_z at fixed Berry curvature dipole P_x and as a function of P_x at fixed Φ_x. Our numerical results match our analytic calculations precisely.

We can interpret this result by noting that the momentum current in Eq. (54) can be obtained in the semiclassical limit by considering the momentum current carried by electron wave packets subject to an anomalous velocity [84,85].

The equation of motion of an electron wave packet with momentum k formed from a single band is

$$v^i(k) = \frac{\partial E}{\hbar \partial k_i} + \frac{e}{\hbar}\epsilon^{ij} E_j F^{xy}(k); \tag{56}$$

where $v^i(k)$ is the wave packet velocity, $E(k)$ is the energy spectrum of the band, E_j is the electric field, and $(e/\hbar)\epsilon^{ij} E_j F^{xy}(k)$ is the anomalous velocity. The momentum current of the occupied states is obtained by adding up the contributions $\hbar k_i v^j(k)$ in the BZ and contains a term arising from the anomalous velocity given by

$$J^i_\lambda = -\frac{e}{(2\pi)^2}\epsilon^{ij} E_j \int d^2k k_\lambda F^{xy}(k_x, k_y)$$
$$= -\frac{e}{4\pi} P_\lambda \epsilon^{ij} E_j : \tag{57}$$

We can also numerically probe our response equations by studying the charge response to the deformation of the lattice. To do so, we introduce a translation flux to rows of plaquettes located near $y = N_y/4$ and $y = 3N_y/4$, analogous to the magnetic flux configuration we just considered. This effectively inserts two rows of dislocations such that, if one encircles a plaquette containing translation flux, the Burgers vector is in the x direction. This effectively creates opposite translational magnetic fields $B^x_z = \partial_x e^x_y - \partial_y e^x_x$ penetrating the two rows of plaquettes. Again, we choose this geometry since it is compatible with translation symmetry in the x direction. In our lattice model, we insert the translation flux by explicitly adding generalized Peierls' factors that are k_x dependent, i.e., $\exp(ik_x \int_R dx^i e^x_i)$ such that the colored regions in Fig. 4(b) contain nonvanishing translation flux. The resulting electron charge density localized on the translation magnetic flux has a dependence on both the B_z field strength and the Berry curvature dipole moment P_x as shown in Figs. 4(e) and 4(f). This again matches the expectation from our analytic response equations.

We emphasize that the effective action (53) describes the mutual bulk response between the electromagnetic and the momentum currents in semimetallic and insulating systems with vanishing Chern number. We show in Sec. III A 1 that one must be careful when comparing this response to the charge polarization. In particular, our numerics show that, even in the presence of significant inversion breaking, the bulk momentum density response to a magnetic flux tracks the value of the coefficient θ from Eq. (9) as demonstrated in Fig. 4(d). In contrast, as shown in Sec. III A 1, the expression for the electric polarization, Eq. (15), contains an additional term that is proportional to the value of a Wilson loop along the boundary of the BZ. This value is not quantized when inversion symmetry is broken, and, for large values of V_l, this contribution becomes significant enough that the polarization response clearly deviates from

the result one would expect from a naive interpretation of Eq. (53). However, the mutual response between the electromagnetic and translation gauge fields described by this action remains valid. This subtlety is not the focus of our current article, so we leave further discussions to future work.

B. 2D Dirac quadrupole semimetal

Next, we consider the class of 2D semimetallic phases characterized by the quadrupole moment of the Berry curvature introduced in Sec. III A 2. We know from Sec. III A 2 that the low-energy effective response action for this system takes the form

$$S = \frac{\hbar}{8\pi} Q_{\alpha\beta} \int e^{\alpha} \wedge de^{\beta}. \quad (58)$$

This action generates a momentum current response

$$J^{\mu}_{\alpha} = -\frac{\hbar}{4\pi} Q_{\alpha\beta} \varepsilon^{\mu\nu\sigma} \partial_{\nu} e^{\beta}_{\sigma}. \quad (59)$$

These currents describe both a bulk momentum polarization (e.g., yielding momentum on the boundary where $Q_{\alpha\beta}$ changes) and a bulk energy-momentum response to translation gauge fields. We note that this response is exactly analogous to that of the Dirac-node dipole semimetal discussed above if we replace the electromagnetic field with a translation gauge field.

To illustrate and explicitly confirm the responses numerically, we use the following two-band square lattice Bloch Hamiltonian with next-nearest-neighbor hopping terms:

$$H(k) = V_T \sigma^x + \sin(k_x a) \sin(k_y a) \sigma^y + [m - \cos(k_x a) - \cos(k_y a)] \sigma^z. \quad (60)$$

This model has an inversion symmetry (i.e., C_2 symmetry) that is realized trivially on site with $I = I$, mirror symmetry along the $k_x = k_y$ axis, and, when $V_T = 0$, time-reversal symmetry $T = \sigma^z K$. This model can be tuned to a semimetal phase as well; for example, setting $m = 1$, we find four gapless Dirac points located at $(k_x, k_y) = (\pi/2a, 0)$ and $(k_x, k_y) = (0, \pi/2a)$.

To confirm the response action is correct, we first need to calculate the Dirac-node quadrupole moment. To see that the Berry curvature quadrupole moment is well defined, we first note that the choice of V_T as a mass perturbation forces P_{α} to vanish. We also need the Chern number to vanish, which is guaranteed by the mirror symmetry. With these symmetries, the Berry curvature peaks at Dirac points that are related by inversion symmetry have the same sign, while the peaks related by mirror symmetry carry opposite signs, resulting in a quadrupolar distribution of the Berry curvature, as in Fig. 5(b). Since the Chern number and P_{α}

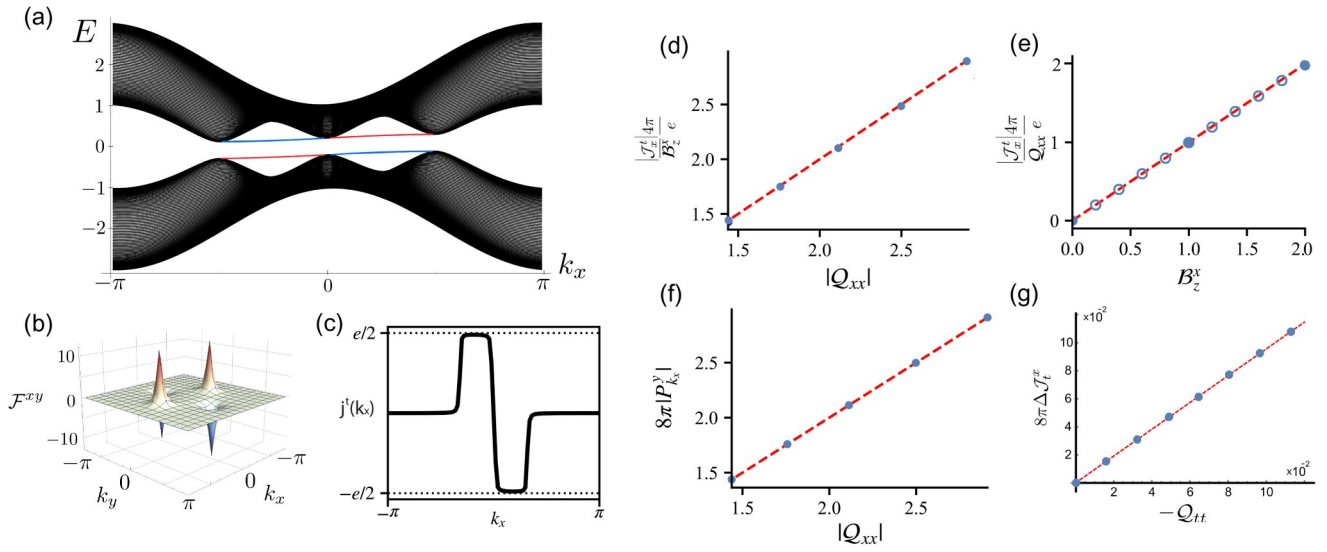

FIG. 5. (a) Spectrum of the 2D Dirac-node quadrupole semimetal (60) in a ribbon geometry (y direction open, x direction periodic) for $m = 1$, the T-breaking perturbation set to $V_T = -0.2$, and the energy tilt in Eq. (62) $\epsilon = 0.1$. At half filling, the ground state of the model is momentum polarized: Occupied states localized near $y = 1$, which are indicated by the blue color, carry a positive value of the k_x momentum, while the occupied states near $y = N_y$ have a negative value of k_x. (b) Berry curvature distribution across the Brillouin zone for a small gapping perturbation $V_T = -0.2$. (c) The boundary charge distribution as a function of momentum. (d),(e) k_x momentum bound to a row of dislocations [cf. Fig. 4(b)] as a function of Q_{xx} at fixed B^x_z in (d) and as a function of B^x_z at fixed Q_{xx} in (e). (f) Plot of momentum polarization $P^y_{k_x}$ obtained from computing k_x-momentum bound to an edge normal to y. (g) As a consequence of nonzero ϵ, we see that the velocities of single-particle states in (a) localized on opposite edges have the same sign, while the energy and k_x momentum charges are exactly opposite. This leads to boundary energy currents as illustrated in (g) as a function of Q_{tt}.

both vanish, the quadrupolar distribution is well-defined and signals the presence of a well-defined elastic response in this model (see also Ref. [75]). The diagonal elements of the Dirac-node quadrupole moment of our model are equal and opposite, $Q_{xx} = -Q_{yy}$, and the off-diagonal elements are zero. Since the sign of the Berry curvature flux for 2D Dirac points with T I symmetry is ambiguous, we once again treat our system in the insulating regime with nonzero V_T first and then recover the semimetallic case by taking the limit $V_T \to 0$.

Using this model, let us first focus on the momentum polarization response and highlight the difference with the 2D Dirac-node dipole semimetal case from Sec. IV A. If the bulk has a momentum polarization, we expect translation-symmetric edges to have a bound momentum density. We first make a general argument for the existence of the boundary momentum and then confirm the results numerically for our model. Let us suppose our system has a boundary normal to the y direction. We expect such a boundary to carry k_x momentum if $Q_{xx} \neq 0$. To show this, let us make a gauge transformation on the fields in Eq. (58): $e^a_\mu \to e^a_\mu + \partial_\mu \lambda^a$ for some vector function λ^a. Since there is a boundary, the response action is not gauge invariant, and we find the variation $\delta_\lambda S = -\delta\hbar Q_{ab}/8\pi \int \partial_0 e^b_x - \partial_x e^b_0$. Our system has no translation twisting of the boundaries, i.e., $e^y_x = e^x_y = 0$, so we find the variation reduces to $\delta_\lambda S = -\delta\hbar Q_{xx}/8\pi \int \partial_0 e^x_x - \partial_x e^x_0$. This variation can be canceled by adding an action of the form Eq. (33). That is, we expect to have 1D degrees of freedom on the boundary that harbor a nonvanishing k_x momentum density captured by an effective 1D quadrupole moment Q_{xx} that matches the value of the 2D quadrupole moment. Interestingly, we note that the coefficient of Eq. (33) is twice that of the variation we need to cancel. Hence, the edge of our system has a fractional momentum density; i.e., a 1D system with the same Q_{xx} would have twice as much momentum. This is analogous to the fractional boundary charge density one finds from the half-quantized electric charge polarization.

We confirm this response numerically by studying the model (60) on a lattice in a ribbon geometry that is open in the ŷ direction and periodic in x̂. Figure 5(a) shows the resulting band structure, for which a gap is opened by a nonvanishing V_T and the occupied states have two symmetrically positioned sets of flat band states: one in an interval having $k_x < 0$ and the other in an interval having $k_x > 0$. The occupied boundary states with $k_x < 0$ (red) are localized near the top ($y = N_y$) boundary, while the occupied boundary states with $k_x > 0$ (blue) are localized near the bottom ($y = 1$) boundary. At half filling, we find that the excess or deficit charge near the boundary depends on k_x as shown in Fig. 5(c). We see that the states at positive and negative k_x are imbalanced, indicating a nonvanishing k_x momentum density on the edge. Indeed, each state between the Dirac nodes contributes an amount to the total edge momentum equal to k_x weighted by a factor of $1/2$, since the particle density on the edge at each k_x in this range is $1/2$. Because states at opposite k_x have opposite excess and deficit probability density, the total sum is nonvanishing and depends on Q_{xx} as shown in Fig. 5(f). We find that the bulk momentum polarization $P^y_{k_x} = \delta\hbar Q_{xx}/8\pi$ matches the numerically calculated boundary momentum density, as expected for a generalized surface-charge theorem [86]. To further probe the response equations, we subject the Dirac-node quadrupole semimetal to the same linear array of dislocations employed in the previous subsection [cf. Fig. 4(b)]. From Eq. (59), we expect to find momentum density localized on dislocations. Since our geometry preserves translation in the x̂ direction, we can compute the amount of k_x momentum bound to dislocations, similar to how we computed the amount of charge bound to dislocations in the previous subsection. We show our results in Figs. 5(d) and 5(e), where we first plot momentum density as a function of Q_{xx} for fixed translation flux B^x_z and then plot momentum density as a function of B^x_z for fixed Q_{xx}. Both results match the analytic value from the response action.

Finally, let us briefly consider a case when the mixed energy-momentum quadrupole moment Q_{ta} is nonvanishing. In this scenario, the effective action (58) implies the existence of a bulk orbital momentum magnetization of

$$M^z_{k_\mu} = -\frac{\hbar}{8\pi} Q_{t\mu}; \tag{61}$$

that manifests as boundary momentum currents, even in equilibrium (note we assume $c = 1$). To generate a nonvanishing $Q_{t\mu}$ in our model (60), we turn on an additional perturbation

$$\Delta H(k) = \epsilon \sin(k_x) I_{2\times 2}. \tag{62}$$

When $m = 1$ and $V_T \to 0^-$, this induces $Q_{tx} = -\pi\epsilon$ and $Q_{tt} = \epsilon^2$, leading to momentum k_x magnetization $M^z_{k_x} = -\delta\hbar/8\pi Q_{tx}$, and bulk energy magnetization, $M^z_{k_t} = -\delta\hbar/8\pi Q_{tt}$, following from Eq. (61). In Fig. 5(g), we plot the boundary energy current response ΔJ^x_t as a function of Q_{tt}. We calculate this quantity by summing the particle current $(1/\hbar)\partial H/\partial k_x$ weighted by the energy $\epsilon(k)$ of each state. The slope of the plot confirms the coefficients predicted in Eq. (61).

C. 3D nodal line dipole semimetal

Heuristically, we can consider nodal 3D semimetals as arising from stacks of 2D Dirac-node dipole semimetals. Furthermore, similar to the 2D case, with inversion symmetry the bulk response action

$$S[A] = eB_{\mu\nu} \int e^\mu \wedge e^\nu \wedge dA \tag{63}$$

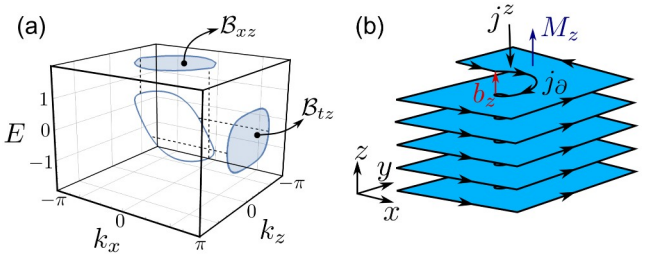

FIG. 6. (a) Fermi line of a 3D NLSM (68) with $V_i = 0$, $m = 2$ that is tiled in the energy-momentum space $\{k_z, k_x, E\}$ by the perturbation (70) where we set $c = 1$. The projections of this curve onto the $\{k_x, k_z\}$ and $\{k_z, E\}$ planes give the exact values of the B_{xz} and B_{tz} coefficients, respectively. (b) A screw dislocation characterized by a Burgers vector $\mathbf{b} = a_z\hat{z}$ creates an internal boundary carrying a current circulating around the magnetization vector M_z. Note that the currents' direction is perpendicular to the Burgers vector and the magnetization vector M_z, as predicted by Eq. (71).

can be interpreted as a charge magnetization M and electric polarization P:

$$eB_{ta} = M^i e^a_i; \qquad eB_{ab} = \epsilon_{ijk} P^k_e e^a_i e^b_j; \tag{64}$$

where we take functional derivatives of Eq. (63) with respect to the magnetic and electric fields, respectively, and use $e^i_i = 1$. For an unmodified geometry we recover the results of Ref. [35], i.e.,

$$eB_{ta} = M^a; \qquad eB_{ab} = \epsilon_{abk} P^k_e. \tag{65}$$

Microscopically, the coefficient B_{ab}, where $a, b = 1, 2, 3$, is proportional to the area of the line nodes that project onto surfaces normal to the ab plane as illustrated in Fig. 6(a).

The bulk action also implies a nonvanishing momentum response to electromagnetic fields:

$$J^\mu_\lambda = 2eB_{\lambda\eta}\epsilon^{\mu\nu\rho\sigma} e^\eta_\nu \partial_\rho A_\sigma \tag{66}$$

and a conjugate electromagnetic response to translation gauge fields:

$$j^\mu = 2eB_{\lambda\eta}\epsilon^{\mu\nu\rho\sigma} e^\lambda_\nu \partial_\rho e^\eta_\sigma. \tag{67}$$

To illustrate how these responses manifest in an explicit model, we can construct a Hamiltonian for a 3D nodal line dipole semimetal by stacking copies of the 2D Dirac-node dipole semimetal in Eq. (55) in the $\hat{z}$ direction. When there is no hopping between the 2D layers, such a system has two lines of gapless states spanning the BZ along the k_z direction, located at $(k_x, k_y) = (K, 0)$ (for our model). Adding hopping terms in the $\hat{z}$ direction leads to a Bloch Hamiltonian:

$$H(k) = V_i \sigma^x + \sin(k_y a_y)\sigma^y + [m - \cos(k_x a_x) - \cos(k_y a_y) - \cos(k_z a_z)]\sigma^z. \tag{68}$$

Taking $V_i \to 0$ and $m = 2$, we find a single loop of gapless states located in the $k_y = 0$ plane, described by the equation $\cos(k_x a_x) + \cos(k_z a_z) = 1$. The stack of 2D Dirac-node dipole semimetals naturally endows the 3D nodal line system with electric polarization (and/or magnetization). Correspondingly, this model has a single nonzero component of the antisymmetric tensor B_{xz} defined in Eq. (36), which encodes a charge polarization in the $\hat{y}$ direction. From Eq. (66), a nonvanishing B_{xz} also implies a k_x momentum line density localized on a magnetic flux tube oriented in the $\hat{z}$ direction:

$$J^t_x = 2eB_{xz}\epsilon^{tzij} e^z_z B_z = 2eB_{xz}B^z; \tag{69}$$

similar to a stack of decoupled 2D Dirac semimetallic layers (in the last equality, we replace $e^z_z \to 1$). This is the 3D analog of the response shown in Figs. 4(c) and 4(d) for the 2D Dirac semimetal.

We can see an example of a charge response if we tilt the nodal line to introduce a nonzero value of B_{tz} as illustrated in Fig. 6(a). In our model, we can tilt the node by adding an extra dispersion

$$\Delta H(k) = \epsilon \sin(k_x a_x) I_{2\times 2} \tag{70}$$

to the Hamiltonian. This term breaks T and induces a net magnetization $M_z = eB_{tz}$, setting up the corresponding circulating boundary currents in the system [35].

Now, when B_{tz} is nonvanishing, Eq. (67) implies that a screw dislocation with Burgers vector $\mathbf{b} = b^z\hat{z}$ hosts a bound electromagnetic current. Indeed, if we assume the screw dislocation is located at $(x, y) = (0, 0)$ and runs along the z axis, we find

$$j^z = -2eB_{tz}\epsilon^{tzjk} e^t_t \partial_j e^z_k = -2eB_{tz} b^z \delta(x)\delta(y); \tag{71}$$

where we use $e^t_t = 1$ and $\nabla \times e^z = b^z\delta(x)\delta(y)$.

We can illustrate the origin of this current by considering the magnetization M_z (and associated boundary currents) induced by B_{tz}. A screw dislocation with Burgers vector $\mathbf{b} = b^z\hat{z}$ can be constructed by cutting a seam into layers normal to $\hat{z}$ and regluing them along the seams with neighboring layers above or below. When cut, the boundary current associated to M_z appears, and after regluing this current is routed vertically along the screw-dislocation line, i.e., along the z direction as shown in Fig. 6(b). The magnetization M_z gives rise to a surface bound current $j_\partial = M_z$

circulating around the $\hat{z}$ axis in each layer. The effective number of current loops winding around the dislocation line per unit length is equal to the Burgers vector. Thus, the total current in the $\hat{z}$ direction is

$$j^z = -b^z j_\partial = -2eB_{tz}b^z; \quad (72)$$

which reproduces the result obtained from the response action. Furthermore, we can understand the sign of the current from Fig. 6(b), where we see that the current on the dislocation has an opposite orientation to the current generated by M_z. Another interesting consequence of Eq. (63) is the topological piezoelectric effect discussed in Ref. [62].

D. 3D nodal line quadrupole semimetal

In Sec. III C, we derive the effective response action

$$S = \hbar B_{\lambda\eta;\alpha} \int e^\lambda \wedge e^\eta \wedge de^\alpha$$

for the nodal line quadrupole semimetal. The response action implies the energy-momentum currents

$$J^\mu_\lambda = 2\hbar(B_{\lambda\eta;\alpha} - B_{\eta\alpha;\lambda})\epsilon^{\nu\rho\sigma}e^\eta_\nu \partial_\rho e^\alpha_\sigma; \quad (73)$$

where we use that $B_{\lambda\eta;\alpha}$ is antisymmetric under exchange of the first two indices.

In analogy with the 2D Dirac-node dipole and Dirac-node quadrupole semimetals, we expect that most of the responses from the Dirac nodal line dipole semimetal in Sec. IV C can be translated to describe some of the responses of this action if we replace charge currents and densities with momentum currents and densities, etc. Indeed, we show in Eq. (38) that, when λ and η are both spatial indices, $B_{\lambda\eta;\lambda}$ implies a momentum polarization in a direction perpendicular to λ and η and carrying momentum parallel to λ. By analogy, the mixed temporal-spatial components $B_{it;j}$ describe a momentum magnetization in the ith direction carrying momentum in the jth direction. The momentum magnetization is further responsible for generating bound currents on screw dislocations; i.e., the momentum magnetization has circulating boundary momentum currents and a momentum current along screw dislocations similar to the charge bound currents on dislocations shown in Sec. V C.

To be more explicit, we can illustrate the momentum polarization in a model by showing the analog of the surface charge theorem; i.e., momentum polarization yields surface momentum densities. To obtain a Hamiltonian for the nodal line quadrupole semimetal, we begin by stacking 2D Dirac-node quadrupole semimetals [see Fig. 5(b)] along the $\hat{z}$ direction. When the planes are completely decoupled, this construction produces a set of four straight Fermi lines stretching in the k_z direction. If we couple the two-dimensional planes, then we arrive at the following Bloch Hamiltonian:

$$H(k) = V_T\sigma^x + \sin(k_x a)\sin(k_y a)\sigma^y + [m - \cos(k_x a) - \cos(k_y a) - \cos(k_z a)]\sigma^z: \quad (74)$$

For a wide range of parameters, this model has a pair of nodal line loops that form a cage structure as shown in Figs. 2 and 7 with $m = 2$ and $V_T = 0$. In general, the local gaplessness of the nodal loops can be protected by the product TI. The cage structure created by the joined, intersecting loops can be split apart by, for example, breaking mirror symmetry along the $k_x = k_y$ axis while preserving TI. However, even in this case, the nodal loops still produce a nonvanishing contribution to the response coefficient $B_{\alpha\beta;\gamma}$. Hence, the response is more general than the specific cagelike nodal configuration. Calculating the response coefficients for the action in the limit $V_T \to 0^-$, we find that $B_{xz;x} = -B_{zx;x}$, $B_{yz;y} = -B_{yz;y}$ are nonvanishing, as shown in Fig. 7.

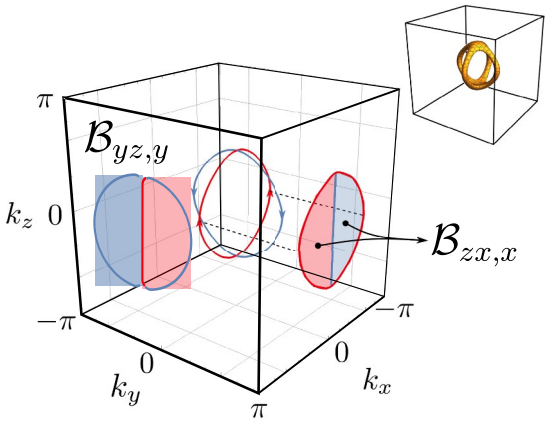

FIG. 7. Fermi lines of the model (74) with $m = 2$ and $V_T \to 0^-$. Resolving this structure as a pair of loops with fixed orientation, we can project them onto the k_xk_z or k_yk_z surfaces to determine the momentum polarization. The colored regions of the projected nodes indicate flat drumhead states that would appear in open boundary conditions on one boundary (red) or the opposing boundary (blue). By looking at the relative positions of the two areas bounded by the projected loops in the surface BZ, we see that one surface has one sign of the k_x or k_y momentum, and the other surface has the other. For example, for the k_xk_z surface BZ, the projections indicate a dipole moment of k_x momentum polarized along the y direction captured by the response coefficient $B_{zx;x}$. Inset: cagelike nodal Fermi surface in the model (74) with $E_F = 0.2$.

Using this model, we can illustrate the origin of the boundary momentum resulting from the bulk momentum polarization. The discussion is analogous to the calculation of the boundary momentum of the 2D Dirac-node quadrupole semimetal in Sec. IV B. Indeed, the analogy is clear, since the cage nodal structure is just arising from a family

of 2D Dirac-node quadrupoles parametrized by k_z. To specify an unambiguous momentum polarization, we turn on a small T-breaking perturbation V. After doing this, and as shown in Fig. 7, we see that the two nodal loop segments that lie in the $k_y = 0$ plane (one for $k_x > 0$ and one for $k_x < 0$) carry the same Berry flux in the z direction (red arrows in Fig. 7). Similarly, the two loop segments in the $k_x = 0$ plane carry the same Berry flux (blue arrows), which is opposite to that carried by the $k_y = 0$ segments. Consequently, the loop segment in the $y = 0$, $k_x > 0$ half plane must connect with a loop segment in the $x = 0$ plane in order to form a closed nodal loop with a consistent helicity or flux sign.

To clarify the consequences of this nodal configuration, let us consider the k_x-k_z plane in Fig. 7. We can calculate a Berry-Zak phase [25] in the k_y direction parametrized by (k_x, k_z), and for our model we find a Berry phase of magnitude π inside the projected nodal region in the k_x-k_z plane. When V is turned on, the signs of the π Berry-Zak phases are no longer ambiguous and are opposite for the projected areas at $k_x > 0$ and $k_x < 0$. If we calculate the total polarization in the y direction when summed over all k_x and k_z, it vanishes. However, the polarization weighted by the k_x momentum is nonzero. The occupied drumhead surface states in the k_x-k_z surface BZ [see Fig. 7 and cf. Figs. 5(a)–5(c)] have an imbalance of k_x momentum but, when combined with the bulk charge density, a vanishing charge [cf. Fig. 5(c)]. This is a reflection of the surface charge theorem for a vanishing charge polarization and nonvanishing momentum polarization. We numerically calculate the magnitude of the bound surface momentum, finding it to be in agreement with the value predicted by the response action, $2\hbar B_{xz;x}$. We see from this picture that, to have a nonzero response $B_{xz;x}$, we want two oppositely oriented nodal loops with identical, nonvanishing areas when projected in the k_x-k_z plane but positioned so that the sums of all k_x inside each nodal loop are different from each other; e.g., in our model, they are opposite values.

As an additional explicit example of a nonvanishing response allowed in our model, we can consider the momentum density

$$J^0_x = 2\hbar B_{xz;x}\epsilon^{ijk}(2e^z_i\partial_j e^x_k - e^x_i\partial_j e^z_k) \tag{75}$$

generated by a geometric deformation. To generate a nonvanishing response, let us consider an xz-planar interface. Since we must preserve translation symmetry along x to calculate k_x momentum, and we want to preserve translation in z for convenience, we have the following terms:

$$J^0_x = 2\hbar B_{xz;x}(2e^z_x\partial_y e^x_z - 2e^z_z\partial_y e^x_x - e^x_x\partial_y e^z_z + e^x_z\partial_y e^z_x).$$

If we cut the system at $y = 0$, both sides of the interface carry a surface k_x-momentum density $J^0_{x;\mathrm{surf}} = 2\hbar B_{xz;x}$, since the system has a k_x momentum polarization along $\hat{y}$ with this magnitude. Since each interface carries an opposite sign of the momentum density, if we glue them back together, there will be no momentum at the interface. Now, for $y > 0$ let us perturb away from the background translation gauge field configuration to $e^a_i = (\delta^a_i + \epsilon^a_i)\Theta(y) + \delta^a_i\Theta(-y)$, where $\epsilon^a_i = (\epsilon^x, 0, \epsilon^z)\Theta(y)$ is a small deformation. The momentum density response to leading order in this is

$$J^0_x = 2\hbar B_{xz;x}(-2\epsilon^x\delta(y) - \epsilon^z\delta(y)); \tag{76}$$

which we see is localized at the interface $y = 0$.

We can interpret this response by noting that changing e^x_x or e^z_z effectively changes the area of one side of the interface ($y > 0$) relative to the other ($y < 0$). Since the total k_x momentum on both sides of the interface should be unchanged by this deformation (we maintain translation symmetry in x during the process), then increasing the area for $y > 0$ must lower the momentum density. Indeed, the surface k_x momentum density on $\hat{y}$ surfaces must be inversely proportional to L_x and L_z. Finally, since we are considering k_x-momentum density, the quantization of which depends on L_x^{-1}, J^0_x actually depends on $L_x^{-\beta}$, hence the difference between the coefficients of ϵ^x and ϵ^z in Eq. (76).

E. 3D Weyl-node dipole semimetal

The electromagnetic and geometric response of time-reversal-breaking 3D Weyl semimetals have been discussed extensively in the literature [12,13,15–21,23,33,34,71,72,87–97]. Here, we focus on a few particular consequences of the mixed crystalline-electromagnetic response and the matching between the response field theory and microscopic lattice model calculations. Recall that the response action for a 3D Weyl semimetal with a nonvanishing Weyl-node dipole moment P_λ is

$$S = \frac{e^2 P_\lambda}{8\pi^2\hbar}\int e^\lambda \wedge A \wedge dA. \tag{77}$$

This response implies the following bulk electromagnetic and momentum currents:

$$j^\mu = -\frac{e^2 P_\lambda}{4\pi^2\hbar}\varepsilon^{\mu\nu\rho\sigma}e^\lambda_\nu\partial_\rho A_\sigma + \frac{e^2 P_\lambda}{8\pi^2\hbar}\varepsilon^{\mu\nu\rho\sigma}A_\nu\partial_\rho e^\lambda_\sigma; \tag{78}$$

$$J^\mu_\lambda = \frac{e^2 P_\lambda}{8\pi^2\hbar}\epsilon^{\mu\nu\rho\sigma}A_\nu\partial_\rho A_\sigma. \tag{79}$$

In the presence of dislocations, the translational flux is nonvanishing, and, hence, the bulk electromagnetic current is anomalous:

$$\partial_\mu j^\mu = -\frac{e^2 P_\lambda}{8\pi^2\hbar}\varepsilon^{\mu\nu\sigma\rho}\partial_\mu e^\lambda_\nu\partial_\sigma A_\rho. \tag{80}$$

This reflects the fact that the action Eq. (77) is not gauge invariant in the presence of dislocations. Indeed, in our explicit tight-binding model calculations below, we find the spectrum on a single screw dislocation line contains a pair of chiral modes of the same chirality [one near each bulk Weyl-node momentum as shown in Fig. 9(b)]. These modes are responsible for the anomalous current on dislocation lines, as was first described by Ref. [38].

To verify the electromagnetic response to the applied crystalline gauge field, we consider a simple two-band model of a 3D Weyl semimetal with a pair of gapless nodes

$$H(k) = \sin(k_z a_z)\sigma^z + \sin(k_y a_y)\sigma^y + [2 - m - \cos(k_x a_x) - \cos(k_y a_y) - \cos(k_z a_z)]\sigma^z.$$

The Weyl node with the positive chirality $\chi = +1$ is located at $k = (\arccos(-m), 0, 0)$, and the node with $\chi = -1$ is at $k = (-\arccos(-m), 0, 0)$. The Weyl-node dipole moment, therefore, has only one nonzero component $P_x = 2\arccos(-m)$, and the resulting response action is

$$S[A_\mu, e^x_\nu] = \frac{e^2 P_x}{8\pi^2\hbar}\int d^4x\, \epsilon^{\mu\nu\rho\sigma} e^x_\mu A_\nu \partial_\rho A_\sigma. \quad (81)$$

Let us first consider the response arising from the constant background translation fields $e^x_x = 1$ and $e^x_y = b^x/L_y$, which describe a twist such that a particle traversing the lattice in the y direction translates by b^x in the x direction. We note that such a configuration is volume preserving, since $\det(e) = 1$, where the matrix e has matrix elements $e^i_j = e^i_j$. When $b^x = 0$, the response action is

$$\frac{e^2 P_x}{8\pi^2\hbar}\int d^4x\, e^x_x \epsilon^{x\nu\rho\sigma} A_\nu \partial_\rho A_\sigma.$$

Using the relation $\int_R dx\, e^x_x = L_x$, we find an anomalous Hall effect in the yz plane such that $\sigma_{yz} = (e^2/h)(P_x L_x/2\pi)$, which is the standard result [32,33]. Now, if we turn on b^x, we still have the same σ_{yz}, but we also have the additional term

$$\frac{e^2 P_x}{8\pi^2\hbar}\int d^4x\, e^x_y \epsilon^{y\nu\rho\sigma} A_\nu \partial_\rho A_\sigma.$$

Because of the different index on the ϵ symbol, this term represents an anomalous Hall effect in the xz plane with $\sigma_{zx} = (e^2/h)(P_x b_x/2\pi)$. We can find a simple interpretation for this effect: When we turn on e^x_y, the minimal coupling $k_x \to k_x$; $k_y \to k_y + k_x e^x_y$ shifts the bulk Weyl nodes, $(P_x, 0, 0) \to (P_x, P_x b_x/L_y, 0)$. Hence, an effective $P_y = (P_x b_x/L_y)$ is generated when the Weyl momenta are sheared. Indeed, we expect that, at least for uniform, traceless translation gauge field deformations, the response phenomena can be simply interpreted as transformations of the Weyl-node dipole $P_i \to e^j_i P_j$. We show an explicit example of this in the first and third surface-BZ panels in Fig. 8(a), where the bulk nodes and their connected Fermi arcs are rotated in the deformed geometry relative to the undeformed geometry. We note that if the deformation is not volume preserving, then we must be careful when considering what is held fixed while volume is changing in order to interpret the resulting phenomena.

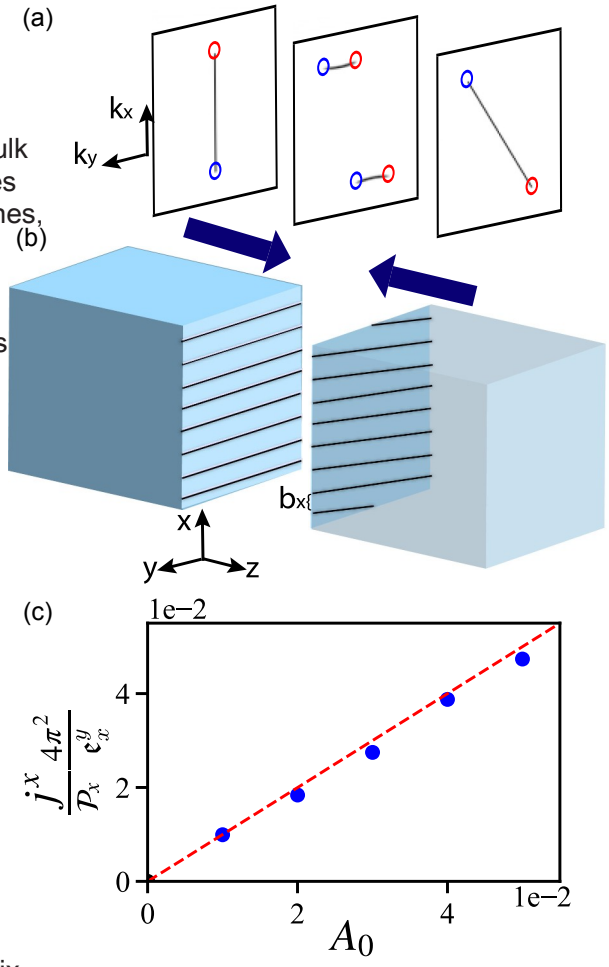

FIG. 8. (a) The three panels show numerically calculated Fermi arcs in (left) the surface BZ with undeformed geometry, (right) the surface BZ with e^x_y nonvanishing, and (center) the arcs localized at the interface formed by gluing the two sides of the interface together. The colored circles in the first and third panels represent the surface BZ projections of the bulk Weyl nodes on either side of the interface. The color is a guide to show the connectivity or orientation of the Fermi arcs, not the chirality of the bulk nodes. On both sides of the interface, the bulk nodes have the same chirality, but, since they are effectively projected onto surfaces having opposite normal vectors, they generate Fermi arcs having opposite chirality. (b) Illustrations of (left) the undeformed geometry and (right) the deformed geometry with e^x_y nonvanishing. (c) The numerically calculated current localized at the interface between undeformed and deformed geometries as a function of the chemical potential shift A_0.

In addition to these cases of fixed background translation fields, let us consider varying those fields in space. We are interested in the electromagnetic response to applied translational magnetic fields $B_i = \epsilon^{ijk}\partial_j e^a_k$. Since the nodes in our model are separated in k_x, we consider geometries where the Burgers vector of the translation magnetic field also points along the x direction, $B_i^x \neq 0$.

First, let us consider a system containing a domain wall as a function of z, such that at $z = 0$ the $\hat{y}$ lines map from 0 to $b_x = L_y$. For $z < 0$ we have bulk Weyl nodes that project onto the z surface at $(P_x = 2, 0)$, while for $z > 0$ the bulk Weyl nodes have been transformed and sit at $(\frac{1}{2}P_x = 2, P_x b_x = (2L_y)$. We show the numerically calculated Fermi arcs for our undeformed and deformed models in the left and right surface BZ panels, respectively, in Fig. 8(a).

Now let us glue the $z < 0$ and $z > 0$ sides to each other to make a domain-wall interface. We schematically illustrate the interface geometry in Fig. 8(b). Since the normal vector on each side of the interface is opposite, we expect the Fermi arcs for $z < 0$ to have the opposite chirality to their corresponding arcs for $z > 0$. Indeed, as shown in the center surface BZ panel in Fig. 8(a), the Fermi arcs on both sides can hybridize because of their opposite chiralities and form new arcs in the 2D subsystem of the interface. These new Fermi arcs encode the fact that the Hall conductivity σ_{xz} is varying at this interface. These effects are all manifestations of the fact that the Weyl-node dipole moment P_i is changing at the interface, and, hence, we expect Fermi arcs to be trapped generically at the interfaces of this type. We note that a similar strain geometry, and the corresponding Weyl-node configuration, was discussed in Ref. [61].

From Eq. (78), we see that applying a uniform, nonvanishing A_0 to the system described above should generate a charge current in the x direction. We can see the microscopic origin of this current as follows. If we increase A_0, each linearly dispersing point on the Fermi arc has an excess charge density $\delta n(k) = \frac{1}{2}\frac{e}{2\pi\hbar}|v_F(k)|$, where $v_F(k)$ is the Fermi velocity at the Fermi arc located at k in the surface BZ. Hence, the contribution to the current of such a point on the Fermi arc is $j^x(k) = e v_F(k)\delta n(k)$.

For our model and geometry, the contributions to the j^x current that are linear in the deformations arise from the Fermi arcs stretching between $(K, 0) \to (K, K_y^x)$ and $(-K, 0) \to (-K, -K_y^x)$. Each of these arcs has a fixed value $k_x = K$, and each arc has an opposite Fermi velocity. Hence,

$$j^x = e v_F(K, k_y)\delta n\frac{K e_y^x}{2\pi} + e v_F(-K, k_y)\delta n\frac{K e_y^x}{2\pi} = \frac{e^2 P_x e_y^x A_0}{4\pi^2\hbar}\mathrm{sgn}(v_F),$$

where $K_y = 2\pi$ counts the density of states on the Fermi arc in the k_y direction, $\mathrm{sgn}(v_F)$ is sign of the velocity on the $k_x = +K$ arc, and $P_x = 2K^2$ is the undeformed value. This result matches the prediction from the response theory and matches the numerical results in Fig. 8(c) [98].

We can also study a system with a pair of screw dislocation lines. We explicitly insert two screw dislocations at positions $(y, z) = (\frac{1}{4}L_y, 0)$ and $(y, z) = (\frac{3}{4}L_y, 0)$, running parallel to the $\hat{x}$ axis with Burgers vectors $b^x = +1$ and $b^x = -1$, respectively. In Fig. 9(a), we show the energy spectrum of a Weyl semimetal with Weyl nodes on the k_x axis with periodic boundary conditions and no dislocations. In Fig. 9(b), we show the spectrum of the same system after two screw dislocations are inserted as described above. The blue and red coloration indicates on which dislocation the states are localized. We see that near each Weyl point the right-moving modes are on the red dislocation, while the left-moving modes are on the blue dislocation, as described by Eq. (78). Hence, each dislocation has a net chirality.

To test the response equation, we apply a nonvanishing A_x and numerically calculate the charge density localized on a single dislocation. We can carry out a microscopic calculation of the charge bound to a dislocation as a function of A_x. Let us assume a nodal configuration with a positive node at $k = (P_x = 2, 0)$ and a negative node at $(-P_x = 2, 0)$. In the presence of a dislocation having Burgers vector b^x, each $k_y k_z$ plane sees an effective

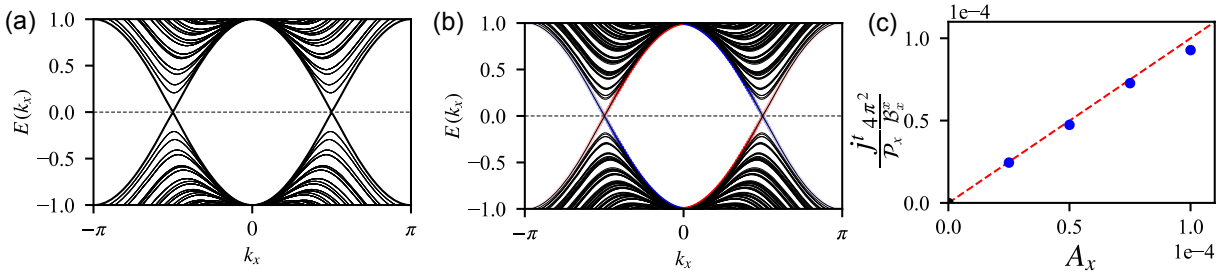

FIG. 9. (a) The bulk spectrum of a Weyl semimetal with two nodes on the k_x axis. (b) The spectrum of the same Weyl semimetal with periodic boundary conditions and two screw dislocations with opposite Burgers vectors threaded along the x direction. Red and blue coloration indicates on which dislocation the chiral modes are localized. Each dislocation has a net positive (red) or negative (blue) chirality. (c) Numerical calculation of the charge density bound to a screw dislocation as A_x is tuned.

magnetic flux $\Phi(k_x) = (k_x/2\pi)\Phi_0$, where $\Phi_0 = h/e$. Hence, each $k_y k_z$ plane having a nonvanishing Chern number contributes to the charge as

$$\Delta Q = \frac{eL_x}{2\pi}\int_{BZ} C(k_x)\frac{k_x b^x}{2\pi}dk_x = 0; \quad (82)$$

where $C(k_x)$ is the Chern number of each $k_y k_z$ plane parametrized by k_x. If we turn on a nonvanishing A_x ($k_x \to k_x + (e/\hbar)A_x$) and recalculate the bound charge, we find

$$\Delta Q|_{A_x} = -\frac{L_x}{2\pi}\int_{-\delta P_x=2\pi-(e/\hbar)A_x}^{\delta P_x=2\pi-(e/\hbar)A_x}\frac{k_x b^x}{2\pi}dk_x = \frac{e^2 P_x b^x L_x}{4\pi^2\hbar}A_x. \quad (83)$$

This result is exactly what is found in our numerics shown in Fig. 9(c). Both of these results match the analytic prediction in Eq. (78) after including an extra factor of 2 which takes into account the bulk and boundary inflow to the boundary [73,99–101].

F. 3D Weyl-node quadrupole semimetal

Finally, we discuss some aspects of the crystalline response of 3D Weyl semimetals with gapless Weyl nodes forming a quadrupole pattern. Some of these responses were recently discussed in Refs. [17,18,24], and here we consider some of the responses in more microscopic detail and compare directly with lattice model calculations.

Recall from Sec. III E the response action

$$S_{WQ} = \frac{eQ_{\alpha\beta}}{8\pi^2}\int e^\alpha \wedge de^\beta \wedge A.$$

The bulk linear response implied by Eq. (49) is

$$J^\mu_\alpha = \frac{e}{8\pi^2}\varepsilon^{\mu\nu\rho\sigma}Q_{\alpha\beta}e^\beta_\nu\partial_\rho A_\sigma - \frac{e}{4\pi^2}\varepsilon^{\mu\nu\rho\sigma}Q_{\alpha\beta}A_\nu\partial_\rho e^\beta_\sigma; \quad (84)$$

$$j^\mu = -\frac{e}{8\pi^2}\epsilon^{\mu\nu\rho\sigma}Q_{\alpha\beta}e^\alpha_\nu\partial_\rho e^\beta_\sigma. \quad (85)$$

We also note that both of these currents can be anomalous when subjected to certain gauge field configurations:

$$\partial_\mu J^\mu_\alpha = -\frac{e}{8\pi^2}\varepsilon^{\mu\nu\rho\sigma}Q_{\alpha\beta}\partial_\mu e^\beta_\nu\partial_\rho A_\sigma; \quad (86)$$

$$\partial_\mu j^\mu = -\frac{e}{8\pi^2}\epsilon^{\mu\nu\rho\sigma}Q_{\alpha\beta}\partial_\mu e^\alpha_\nu\partial_\rho e^\beta_\sigma. \quad (87)$$

Now let us consider several different phenomena associated to these response equations in the context of a lattice model introduced in Ref. [17]:

$$H(k) = \sin k_x \sin k_y \Gamma^x + \sin k_z \Gamma^y + [m + t(\cos k_x + \cos k_y + \cos k_z)]\Gamma^z. \quad (88)$$

Without any geometric deformations, the semimetal phase of our model with a Weyl-node quadrupole has two nodes of one chirality at $k = (K, 0, 0)$ and two of the opposite chirality at $(0, K, 0)$. Thus, the gapped 2D $k_y k_z$ planes parametrized by k_x have a nonvanishing Chern number C for $-K < k_x < 0$ and a nonvanishing Chern number $-C$ for $0 < k_x < K$, where $C = 1$. Similar statements can be made about the $k_x k_z$ planes. Without loss of generality, let us choose the nodes on the k_x axis to have positive chirality such that $Q_{xx} > 0$ and $C = +1$. For our model, this also implies that $Q_{yy} < 0$ and the nonvanishing $k_x k_z$ Chern number planes have a negative Chern number for $k_y < 0$ and positive Chern number for $k_y > 0$. For example, in our model, we can generate a configuration with this structure using $m = -2, t = 1$.

1. Response to flux and dislocation lines

We begin by studying the momentum density bound to magnetic flux and charge density bound to dislocations. These two responses, some aspects of which are described in Ref. [17] (see also Refs. [18,24]), are the most straightforward, because they are essentially bulk responses and do not generate anomalous currents; i.e., the rhs of the anomalous conservation laws above vanish. Our model has $Q_{xx} = -Q_{yy} \neq 0$, and the responses generated by these two coefficients give two separate sets of terms in the response action. Hence, for simplicity, we consider only the Q_{xx} responses for now.

Let us first microscopically calculate the expected response to inserting a magnetic flux or a screw dislocation and compare with the response theory. First, consider inserting a thin magnetic flux line along the x direction having flux Φ localized at, say, $(y, z) = (0, 0)$. This flux generates a Hall effect from each of the nontrivial $k_y k_z$ Chern planes. The total charge bound to the flux line vanishes, because there are equal and opposite contributions from $k_x < 0$ and $k_x > 0$. However, threading the flux builds up a nonvanishing k_x momentum, since planes with opposite k_x momentum have opposite Chern number. The total momentum (spatial integral of momentum density) driven to the flux line by the Hall effect at each k_x momentum is

$$\Delta P_x = -\frac{\Phi}{\Phi_0}\frac{L_x}{2\pi}\int_{-\pi}^{\pi}dk_x C(k_x)\hbar k_x = \frac{\Phi}{\Phi_0}\frac{\hbar K^2 L_x}{2\pi}; \quad (89)$$

where the Chern number $C(k_x)$ is the piecewise-constant function across the k_x BZ described above and $\Phi_0 = h/e$ is the quantum of magnetic flux. Using the fact that $Q_{xx} = 2K^2$ and dividing by the volume, we find the momentum density

$$J^0_x = \frac{eQ_{xx}}{8\pi^2}B_x. \quad (90)$$

This is the same result coming from the first term in Eq. (84) when $e^x_x = 1$.

Next, let us calculate the charge response to inserting dislocations. Consider a screw dislocation with Burgers vector component b^x associated to a translation gauge field configuration $B^x_x \equiv \partial_y e^x_z - \partial_z e^x_y = b^x \delta(y)\delta(z)$. From Eqs. (84) and (85), we see that both the momentum and charge currents have responses to dislocations, and we first calculate the charge response. Heuristically, the dislocation is like a U(1) gauge flux that couples to momentum instead of electric charge, so the dislocation couples to momentum because it has a nonvanishing k_x. Hence, each $k_y k_z$ plane having a nonvanishing Chern number (and nonvanishing k_x) generates a Hall response, but with a magnitude proportional to its k_x charge. Indeed, each plane sees an effective flux $\Phi(k_x) = (b^x/2\pi)\Phi_0$. Hence, the total charge bound to the dislocation is

$$\Delta Q = \frac{eL_x}{2\pi}\int_{-\pi}^{\pi} dk_x \frac{k_x b_x}{2\pi} C(k_x) = -\frac{eb_x Q_{xx}}{8\pi^2} L_x. \quad (91)$$

This matches Eq. (85), again after setting $e^x_x = 1$ (see also Refs. [17,18,24]).

Now we consider the momentum response to a dislocation, i.e., a momentum density bound to the dislocation when A_x is nonvanishing [this comes from the second term in Eq. (84)]. First, we can compute the amount of momentum bound to a dislocation when $A_x = 0$ by adding the contributions of each Chern plane:

$$\begin{aligned}\Delta P_x &= \frac{L_x}{2\pi}\int_{-\pi}^{\pi} dk_x \frac{k_x b_x}{2\pi} C(k_x)\hbar k_x \\ &= \frac{L_x b_x \hbar}{4\pi^2}\left(\int_0^K dk_x k_x^2 - \int_{-K}^0 dk_x k_x^2\right) \\ &= 0. \end{aligned} \quad (92)$$

We note that this calculation is similar to Eq. (91) except with an additional factor of the "momentum charge" $\hbar k_x$ in the integrand. Now if we turn on an A_x such that $k_x \to k_x + (e/\hbar)A_x$, we can repeat the calculation to find

$$\begin{aligned}\Delta P_x|_{A_x} &= \frac{L_x b_x \hbar}{4\pi^2}\left(\int_{-eA_x/\hbar}^{K-(eA_x/\hbar)} dk_x k_x^2 - \int_{-K-(eA_x/\hbar)}^{-eA_x/\hbar} dk_x k_x^2\right) \\ &= -\frac{eL_x b_x 2K^2}{4\pi^2} A_x. \end{aligned}$$

The final result yields

$$J^0_x = -\frac{eQ_{xx}A_x}{4\pi^2} B^x_x, \quad (93)$$

which matches Eq. (84) and our numerical calculations in Figs. 10(c) and 10(d). For the numerics, we insert a pair of screw dislocations with Burgers vectors $b^x = a_x$ in the presence of a constant background gauge potential A_x. The resulting k_x momentum density of the ground state as a function of the y and z lattice coordinates is shown in Fig. 10(c). Furthermore, the dependence of this momentum density on A_x reproduces the expected response coefficient, as shown in Fig. 10(d).

2. Response of a deformed interface

Next, let us consider an interface between an undeformed geometry and a geometry having a nonvanishing background e^y_x and e^x_y as shown in Fig. 11(b). To be explicit, let the interface between the two geometries occur as a function of z at $z = 0$. On the surface of the undeformed system, we numerically calculate the characteristic (rank-2) Fermi arc structure as shown in the left surface-BZ panel in Fig. 11(a). For our deformed geometry, we show the modified bulk Weyl-node quadrupole and Fermi arcs when $e^y_x = e^x_y \neq 0$ in the right surface-BZ panel in Fig. 11(a).

From these figures, we see that the Weyl-node quadrupole moment $Q^{(R)}_{ab}$ on the deformed side is modified from the quadrupole moment $Q^{(L)}_{ab}$ on the undeformed side. Explicitly, we can compute

$$\begin{aligned} Q^{(R)}_{xx} &= (e^y_x)^2 Q^{(L)}_{xx} + 2e^x_x e^y_x Q^{(L)}_{xy} + (e^y_x)^2 Q^{(L)}_{yy}; \\ Q^{(R)}_{xy} &= e^x_x e^x_y Q^{(L)}_{xx} + e^y_x e^y_y Q^{(L)}_{yy} + (e^x_x e^y_y + e^y_x e^x_y) Q^{(L)}_{xy}; \\ Q^{(R)}_{yy} &= (e^x_y)^2 Q^{(L)}_{xx} + 2e^x_y e^y_y Q^{(L)}_{xy} + (e^y_y)^2 Q^{(L)}_{yy}; \end{aligned} \quad (94)$$

i.e., $Q^{(R)}_{ij} = e^a_i Q^{(L)}_{ab} e^b_j$. For our model and geometry, we can make the simplifications $e^x_x = 1 = e^y_y$, $e^y_x = e^x_y$, $Q^{(L)}_{xy} = 0$, and $Q^{(L)}_{xx} = 2K^2 = -Q^{(L)}_{yy}$. Substituting these relations into Eq. (94) yields

$$Q^{(R)}_{xx} = -Q^{(R)}_{yy} = 2K^2[1 - (e^y_x)^2] \quad (95)$$

and $Q^{(R)}_{xy} = 0$. Alternatively, we can see this result from the locations of the deformed Weyl nodes which sit at $(K, Ke^y_x, 0_+)$, $(-K, -Ke^y_x, 0_+)$, $(Ke^y_x, K, 0_-)$, and $(-Ke^y_x, -K, 0_-)$ (where the subscripts encode the chirality for our choice of model parameters).

Since the Weyl-node quadrupole moments on the two sides of the interface are different, we expect gluing the two sides together to leave behind a signature at the interface. Indeed, from the middle surface-BZ panel in Fig. 11(a), we see gapless Fermi arcs that remain at the interface and

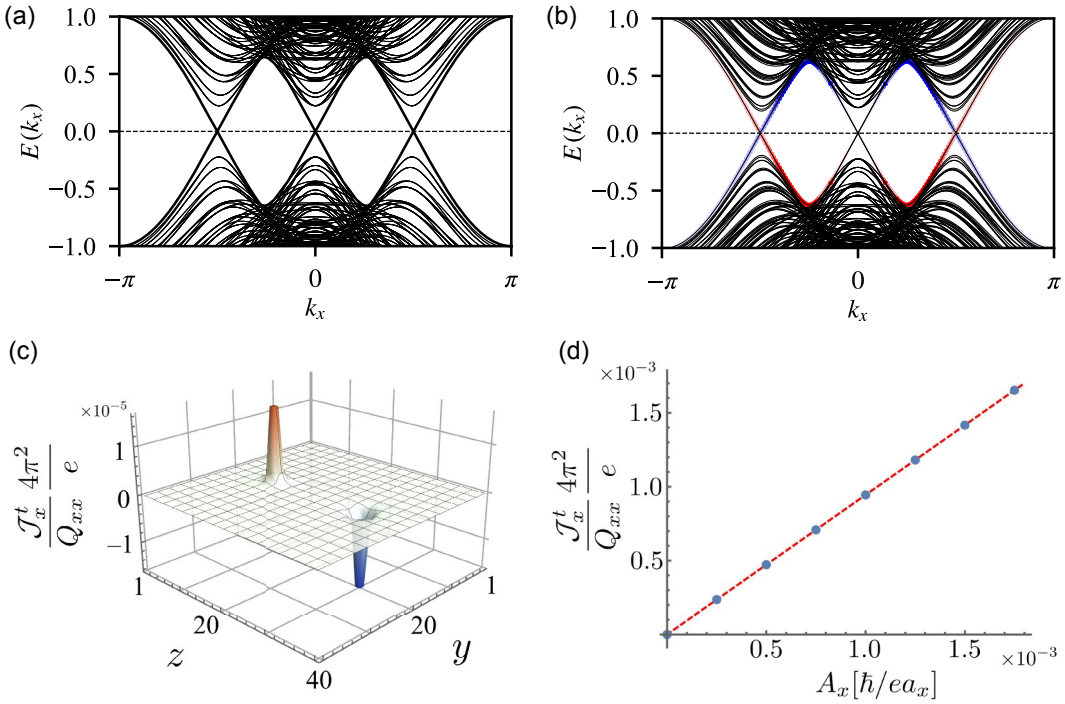

FIG. 10. (a) The bulk spectrum of a Weyl semimetal with two nodes of one chirality on the k_x axis and two nodes of the opposite chirality on the k_y axis. (b) The spectrum of the same Weyl semimetal with periodic boundary conditions and two screw dislocations with opposite Burgers vectors threaded along the x direction. Red and blue coloration indicates on which dislocation the chiral modes are localized. Each dislocation has a no net chirality, and the Weyl nodes on the k_y axis do not form chiral modes. (c) The spatially resolved k_x momentum density response of a Weyl-node quadrupole semimetal to a pair of screw dislocations with opposite Burgers vectors $b_x = a_x$ located at $(y, z) = (20, 20)a_z$ with the background gauge field $A_x = 2.5 \times 10^{-4}\hbar/ea_x$ and $Q_{xx} = \pi^2/2a_x^2$. (d) Numerically calculated dependence of the k_x momentum density localized on a screw dislocation with Burgers vector $b_x = 1$ as a function of the background gauge field A_x, using the same model as in (c).

stretch between the unmodified and modified projected locations of the bulk Weyl nodes. From Eqs. (84) and (85) we see there should be responses

$$J^x_x = -\frac{e}{4\pi^2} Q_{xx} A_0 \partial_z e^x_y; \qquad J^y_y = -\frac{e}{4\pi^2} Q_{yy} A_0 \partial_z e^y_x;$$

$$j^0 = \frac{e}{8\pi^2}(Q_{xx} e^x_x \partial_z e^x_y - Q_{yy} e^y_y \partial_z e^y_x) = \frac{eQ_{xx}}{4\pi^2}\partial_z e^y_x;$$

where in the last equality we substitute in the relations that are specific to our model and interface geometry, which we state above.

We confirm the momentum and charge responses numerically, in particular, the J^x_x responses shown in Fig. 11(c), and we also provide microscopic analytic arguments here. The momentum currents both follow the same logic, so let us consider only J^x_x for now. From the center surface-BZ panel in Fig. 11(a), we see remnant Fermi arcs. If we increase A_0, each linearly dispersing point on the Fermi arc has an excess charge density $\delta n(k) = (eA_0/2\pi\hbar)|v_F(k)|$, where $v_F(k)$ is the Fermi velocity at the Fermi arc located at k in the surface BZ. Hence, the contribution to the k_x momentum current of such a point on the Fermi arc is $\delta J^x_x(k) = \hbar k_x v_F(k)\delta n(k)$. For our model and geometry, the contributions to the J^x_x current that are linear in the deformations arise from the Fermi arcs stretching between $(K, 0) \to (K, K_y e^x_y)$ and $(-K, 0) \to (-K, -K_y e^x_y)$. Each of these arcs has a fixed value $k_x = K$, and each arc has an opposite Fermi velocity. Hence,

$$J^x_x = \hbar K v_F(K, k_y)\delta\left(n - \frac{K_y e^x_y}{2\pi}\right) + \hbar(-K)v_F(-K, k_y)\delta\left(n - \frac{K_y e^x_y}{2\pi}\right) = \frac{eQ^{\delta L}_{xx} e^x_y A_0}{4\pi^2}\mathrm{sgn}(v_F);$$

where $K_y = 2\pi$ counts the density of states on the Fermi arc in the k_y direction, $\mathrm{sgn}(v_F)$ is sign of the velocity on the $k_x = \pm K$ arc, and the undeformed $Q^{\delta L}_{xx} = 2K^2$. This result matches the prediction from the response theory and matches the numerical results in Fig. 11(c).

The calculation of the charge density ρ^t at the interface is simpler, since it comes from the bulk response to a translation magnetic field. At the interface, there is a nonvanishing $B^x_x = -\partial_z e^x_y$ and $B^y_y = \partial_z e^y_x$. Since the $k_y k_z$ planes and $k_x k_z$ planes have nonvanishing Chern numbers, they yield a density response similar to what we find on the dislocation line in Eq. (91). Each k_x state sees an effective magnetic flux

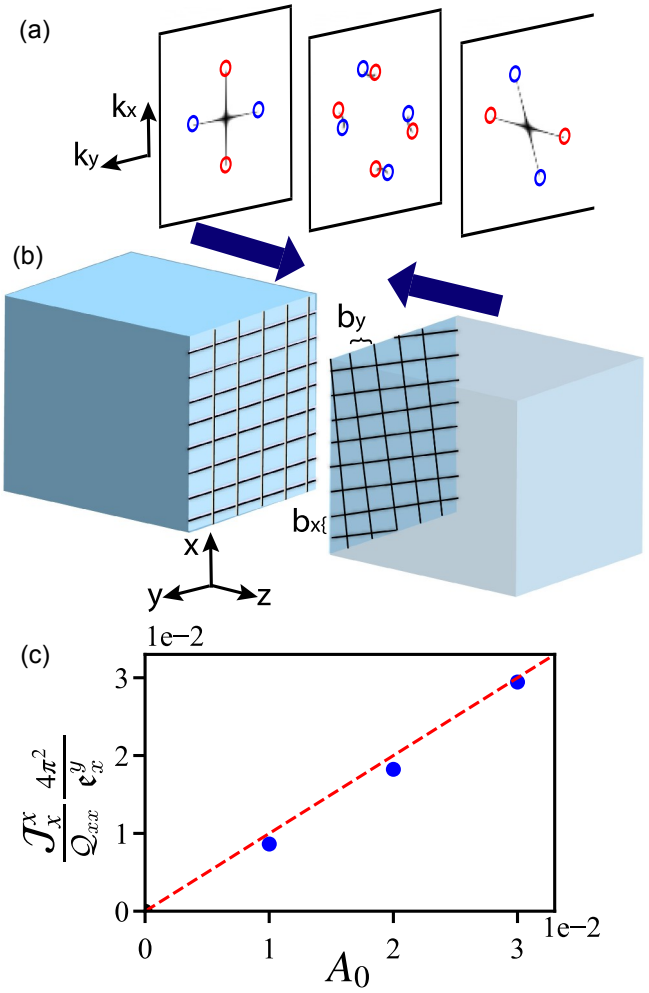

FIG. 11. (a) The three panels show numerically calculated Fermi arcs in (left) the surface BZ of the undeformed geometry, (right) the surface BZ of the deformed geometry with $\mathcal{C}_y^x$ and $\mathcal{C}_x^y$ are nonvanishing, and (center) the BZ of the interface formed gluing the deformed and undeformed geometries together. See the caption in Fig. 8 for comments about the color guides on the open circles representing the surface BZ projections of the bulk Weyl nodes. (b) Illustrations of (left) undeformed and (right) deformed geometries. (c) The numerically calculated momentum current localized at interface between deformed and undeformed geometries as a function of the chemical potential shift A_0.

$\Phi(k_x) = -(k_x b^x/2\pi)\Phi_0$, and similarly for each k_y state $\Phi(k_y) = (k_y b^y/2\pi)\Phi_0$, where $b^x = \int dy\, \mathcal{C}_y^x j_{z>0}$ and $b^y = \int dx\, \mathcal{C}_x^y j_{z>0}$ are the Burgers vectors obtained when integrating across the entire periodic y and x directions, respectively. Hence, the total charge at the interface is

$$\begin{aligned}\Delta Q &= -\frac{2eL_x}{2\pi}\int_0^K dk_x \frac{k_x b^x}{2\pi} + \frac{2eL_y}{2\pi}\int_0^K dk_y \frac{k_y b^y}{2\pi} \\ &= \frac{e}{8\pi^2}(-Q_{xx} b^x L_x + Q_{yy} b^y L_y) \\ &= -\frac{eQ_{xx} b^x L_x}{4\pi^2};\end{aligned}$$

where the leading factors of 2 in the first line account for identical contributions from the intervals $k_x \in [-K, 0]$ and $[0, K]$, and in the last equation we use $Q_{xx} = -Q_{yy}$ and $L_x b^x = L_y b^y$ since $\mathcal{C}_x^y = \mathcal{C}_y^x$. This final result matches Eq. (85).

V. CONCLUSION

In this article, we have presented a framework of explicit connections between a wide-ranging family of topological response theories from 0D to 3D. Using this framework, we have shown how the coefficients for these response theories, most of which are well known in insulators, can be obtained for topological semimetals. This has allowed us to provide careful derivations and characterizations of mixed crystalline-electromagnetic responses of semimetallic and insulating systems in various spatial dimensions. Finally, we have provided an extensive set of microscopic lattice calculations and numerical confirmations affirming that our predicted field theory responses do indeed arise in tight binding lattice models. With the advent of topological quantum chemistry [102–107], thousands of crystalline topological insulators and semimetals have been identified, but many open questions persist about how to probe their topological features. This work provides insight into how the topology in some of these materials may be probed and characterized, i.e., by combining geometric and strain distortions and electromagnetic responses.

There is a growing body of work studying the mixed crystalline-electromagnetic responses of Weyl semimetals with dipole and quadrupole arrangements of nodes [12,13,15–21,23,24,72,88–92,94–97] that indicate a broad interest in these topics. Our work serves two major purposes in the context of this previous literature: (i) We identified several aspects of mixed crystalline-electromagnetic responses that have not yet been addressed in earlier work, and (ii) we synthesized aspects of the existing literature to present a unified description of these responses in terms of the momentum-space multipole moments of the nodal configurations and to provide new intuition in previously studied responses. While prior work has examined the mixed crystalline-electromagnetic response of two-dimensional Dirac-node dipole semimetals [34,64], we have advanced this understanding by identifying a Wilson loop correction the response coefficient that raises a subtle question about the connection between the charge polarization and the mixed-crystalline-electromagnetic response. Additionally, the Dirac-node quadrupole semimetal has not been previously discussed, making our work the first study of its properties and mixed crystalline-electromagnetic responses. Furthermore, our model of a nodal line quadrupole semimetal and its corresponding response theory are new to the literature as well.

The results of this work point in many possible directions for future work. First, finding experimental realizations of the proposed topological responses in solid state or metamaterial systems is an exciting prospect. Rank-2 chiral

fermions, which have an anomaly compensated by the bulk response of a Weyl quadrupole semimetal [17], were realized in a recent experiment on non-Hermitian topoelectric circuit metamaterials [39]. In that platform, the mixed crystalline-electromagnetic response generates a momentum-resolved non-Hermitian skin effect that was observed in the experiment. Topoelectric circuits, along with other metamaterials and solid state platforms, are promising arenas in which the many mixed crystalline-electromagnetic responses we discuss in this paper could be realized. Some of us are also working on extending the nodal, higher-multipole responses to interacting systems and nonequilibrium systems wherein, in the latter, one can have mixed energy-momentum multipole moments. Studying the leading nodal dipole moments has already led to a rich set of phenomena, and the higher moments provide a large hierarchy of phenomena that can be explored in current experiments.

Other extensions of this work include the consideration of additional crystalline gauge fields as was done in, e.g., Refs. [18,48–51,108]. Two important classes of crystalline symmetries that have not yet received such a treatment are nonsymmorphic and orientation nonpreserving crystalline symmetries, both of which can protect exotic topological semimetals [41,109]. It is conceivable that gauge fields for these two classes of crystalline symmetries can be constructed and used to probe the quasitopological responses of semimetals protected by these symmetries. We leave this avenue to future work.

It is also quite interesting to consider responses arising from internal symmetries such as spacetime inversion and chiral symmetry, which protect many unconventional topological semimetals [42–47,110]. Spacetime inversion is antiunitary, so it is unclear if a gauge field can be constructed for it, though it is likely that systems protected by this symmetry would be sensitive to defects of the unitary inversion part of the symmetry and, of course, to the defects of translation symmetry. Chiral symmetry is commonly associated with a sublattice degree of freedom in the UV, while in the IR it can often be connected to a configuration of valleys (or nodal regions). In these scenarios, one can imagine defects of the chiral symmetry arising from a valley-resolved gauge field, strain, or an intrasite field that couples differently to different sublattices. Calculations involving these gauge fields may yield physically meaningful results; however, chiral symmetry is at best approximate in nonsuperconducting systems and, hence, observables tied to these calculations are likely to have significant quantitative differences if considered in experiment.

ACKNOWLEDGMENTS

We thank Lei Gioia and Barry Bradlyn for helpful conversations. T. L. H. acknowledges support by Grant No. NSF PHY-1748958 to the Kavli Institute for Theoretical Physics. F. J. B. is supported by NSF DMR-2313858. T. L. H. and M. R. H. thank ARO MURI W911NF2020166 for support.

APPENDIX A: TRANSLATION GAUGE FIELDS DERIVED FROM THE TELEPARALLEL PRESCRIPTION

In this appendix, we provide a derivation of the translation gauge field e_ν^μ and its coupling prescription that follow directly from gauging the translational symmetry group, which can be done in a similar fashion to gauging the ordinary electromagnetic U(1) symmetry. Consider a translation transformation

$$r^\mu \to r^\mu + a^\mu; \tag{A1}$$

which is generated by corresponding operators $\hat{P}_\mu = -i\hbar\partial_\mu$. Under such an infinitesimal translation, the wave function changes by $\delta\psi = ia^\mu\hat{P}_\mu/\hbar\psi$. Promoting the transformation to a local one, $a^\mu \to a^\mu(r)$, we find that the derivative of ψ does not transform covariantly anymore:

$$\hbar(\partial_\nu\psi) = ia^\mu(r)\hat{P}_\mu\psi + i\hat{P}_\mu\psi\partial_\nu a^\mu(r). \tag{A2}$$

We can compensate the second term by introducing an additional gauge potential B_ν^μ that obeys the gauge transformation rules $B_\nu^\mu \to B_\nu^\mu - \partial_\nu a^\mu(r)$. This allows us to define a covariant derivative:

$$D_\nu\psi = \partial_\nu\psi + iB_\nu^\mu\hat{P}_\mu/\hbar\psi. \tag{A3}$$

Now it is straightforward to check that the covariant derivative transforms as expected:

$$\hbar(D_\nu\psi) = ia^\mu(t, x)D_\nu\hat{P}_\mu\psi. \tag{A4}$$

We can reexpress the partial derivative in Eq. (A3) as a momentum operator to write down:

$$D_\nu\psi = ie_\nu^\mu\hat{P}_\mu/\hbar, \tag{A5}$$

where $e_\nu^\mu = \delta_\nu^\mu + B_\nu^\mu$ is a translation gauge field that inherits its gauge transformations from the gauge potential B:

$$e_\nu^\mu \to e_\nu^\mu - \partial_\nu a^\mu(r). \tag{A6}$$

APPENDIX B: GRADIENT EXPANSION

In this appendix, we do a quick review of the gradient expansion procedure. As we are interested in responses involving both electromagnetic and translation gauge fields, we need to consider how the electron wave vector

gets shifted in the presence of spatially varying gauge fields $A_\mu(r)$ and $\tilde{\beta}(r) = \sum_\mu \beta_\mu B_\mu(r)$ (see Appendix A):

$$k_\mu \to k_\mu + \frac{e}{\hbar} A_\mu(r) + k_\lambda B^\lambda_\mu(r): \quad (B1)$$

For small gauge fields, we can obtain a simple form of the resulting single-particle Green's functions performing a Taylor expansion:

$$\begin{aligned} G_0(k)^{-1} \to G^{-1}_{AB}(k;r) &= G_0^{-1}\left(k_\mu + \frac{e}{\hbar}A_\mu(r) + k_\lambda B^\lambda_\mu(r)\right) \\ &\approx G_0^{-1}(k) + \frac{e}{\hbar}A_\mu(r)\frac{\partial G_0^{-1}}{\partial k_\mu} + k_\lambda B^\lambda_\mu(r)\frac{\partial G_0^{-1}}{\partial k_\mu}(k) + \\ &\approx G_0^{-1}(k) + \frac{e}{\hbar}A_\mu(r) + k_\lambda e^\lambda_\mu(r) - k_\mu \frac{\partial G_0^{-1}}{\partial k_\mu}(k) + : \end{aligned} \quad (B2)$$

We then follow the standard procedure to derive the effective action:

$$\begin{aligned} \frac{i}{\hbar}S &= \log\frac{Z_{AB}}{Z_0} = \log\frac{\mathrm{Det}G^{-1}_{AB}}{\mathrm{Det}G_0^{-1}} \\ &\approx \mathrm{Tr}\log(I + G_0\Sigma); \end{aligned} \quad (B3)$$

where

$$\Sigma = \frac{e}{\hbar}A_\mu(r) + k_\lambda e^\lambda_\mu(r) - k_\mu \frac{\partial G_0^{-1}}{\partial k_\mu}(k) + : \quad (B4)$$

Expanding the trace of logarithm, we get

$$\begin{aligned} \frac{i}{\hbar}S &\approx \mathrm{Tr}\log(I + G_0\Sigma) \\ &\approx \mathrm{Tr}(G_0\Sigma) - \frac{1}{2}\mathrm{Tr}(G_0\Sigma G_0\Sigma) \\ &+ \frac{1}{3}\mathrm{Tr}(G_0\Sigma G_0\Sigma G_0\Sigma) - : \end{aligned} \quad (B5)$$

The rhs of this equation is a sum of integrals over the entire phase space, and the products under functional traces are convolutions. Therefore, we need to use the Moyal product formula, expanding each $G_0\Sigma$ term as

$$G_0 \star \Sigma \approx G_0\Sigma + \frac{i}{2}\{G_0, \Sigma\} + : \quad (B6)$$

where $\star$ is the Moyal product operator and $\{\cdot;\cdot\}$ are the Poisson brackets for the r and k_μ variables [111–113]. The rhs of the last equation contains ordinary products of G_0 and Σ that are subsequently integrated over the phase space. For example, in d spacetime dimensions, we get for the $\mathrm{Tr}(G_0\Sigma)$ term in the 0th order of the Moyal product expansion

$$\int d^d r \int \frac{d^d k}{(2\pi)^d}\left(\frac{e}{\hbar}A_\mu + k_\lambda B^\lambda_\mu\right)\mathrm{tr}\left(G_0\frac{\partial G_0^{-1}}{\partial k_\mu}\right); \quad (B7)$$

where "tr" denotes the ordinary trace over orbital and spin degrees of freedom.

APPENDIX C: ELECTRIC POLARIZATION AS A BERRY CURVATURE DIPOLE

Let us consider the expression for the polarization of a 2D system with a single filled band:

$$P^y_e = \frac{e\Omega}{(2\pi)^2} i\int_{BZ} d^2k \langle u_k|\partial_{k_y}u_k\rangle \equiv \frac{e\Omega}{(2\pi)^2} iP; \quad (C1)$$

where Ω is the area of the unit cell. We rewrite the last integral denoted as P as a first moment of the Berry curvature, $F^{xy} = i\langle\partial_{k_x}u_k|\partial_{k_y}u_k\rangle - i\langle\partial_{k_y}u_k|\partial_{k_x}u_k\rangle$. Consider the following quantity:

$$\begin{aligned} F &= -i\int_{BZ} d^2k\, k_x F^{xy} \\ &= \int_{BZ} d^2k\, k_x\langle\partial_{k_x}u_k|\partial_{k_y}u_k\rangle - \int_{BZ} d^2k\, k_x\langle\partial_{k_y}u_k|\partial_{k_x}u_k\rangle; \end{aligned} \quad (C2)$$

where we assume F^{xy} to be smooth and integrable in the Brillouin zone spanning $k_x \in [-\pi/a_x, \pi/a_x)$ and $k_y \in [-\pi/a_y, \pi/a_y)$. Clearly, the integrand jumps in value at the $k_x = \pi/a_x$ boundary of the Brillouin zone, and so we treat the k_x direction as open. Integrating by parts with respect to k_x we find

$$\begin{aligned} F &= -i\frac{4\pi}{a_x}\int dk_y A^y(k_x = \pi/a_x, k_y) \\ &- \int_{BZ} d^2k\langle u_k|\partial_{k_y}u_k\rangle - \langle\partial_{k_y}u_k|u_k\rangle \\ &- \int_{BZ} d^2k\, k_x\langle u_k|\partial_{k_x}\partial_{k_y}u_k\rangle + \int_{BZ} d^2k\, k_x\langle\partial_{k_x}\partial_{k_y}u_k|u_k\rangle; \end{aligned} \quad (C3)$$

where $A^\mu(k) = i\langle u_k|\partial_{k_\mu}u_k\rangle$ is the Berry connection. The first term is proportional to a Wilson loop $W(k_x = \pi/a_x)$ along the $k_x = \pi/a_x$ line. It is easy to recognize that the second term is twice the integral of interest $-2P$.

Integrating the third and fourth terms by parts with respect to k_y, we find

$$\begin{aligned} &-\int_{BZ} d^2k k_x \langle \partial_{k_x}\partial_{k_y} u_k | u_k\rangle - \langle \partial_{k_x}\partial_{k_y} u_k | \partial_{k_y} u_k\rangle \\ &= \int_{BZ} d^2k k_x \langle \partial_{k_y} u_k | \partial_{k_x} u_k\rangle - \langle \partial_{k_x} u_k | \partial_{k_y} u_k\rangle \\ &= -i \int d^2k k_x F^{yx} = -F: \end{aligned} \quad \text{(C4)}$$

Summing up, we find

$$\begin{gathered} F = -i\tfrac{4\pi}{a_x} W^y - 2P - F \\ \Downarrow \\ P = -F - i\tfrac{2\pi}{a_x} W^y; \end{gathered}$$

and the polarization is, therefore, given by

$$\begin{aligned} P_e^y &= -\frac{e\Omega}{(2\pi)^2}\int_{BZ} d^2k k_x F^{xy} \\ &\quad + \frac{ea_y}{2\pi}\int dk_y A^y(k_x = \pi/a_x; k_y): \end{aligned} \quad \text{(C5)}$$

Performing a similar calculation for P_e^x, we find the general formula

$$P_e^i = \frac{e\Omega}{(2\pi)^2}\varepsilon^{ij}\int d^2k k_j F^{xy} + e a_i W^i: \quad \text{(C6)}$$

In the case when the system has inversion symmetry, the Wilson loop taken along a high-symmetry line satisfies $W^i(k_j = \pi/a_j) = -W^i(k_j = \pi/a_j)$ and $W^i(k_j = 0) = -W^i(k_j = 0)$ for $i \neq j$, and we find that the nonquantized part of the polarization is accounted for entirely by the Berry curvature's dipole moment.

APPENDIX D: MOMENTUM POLARIZATION AS A BERRY CURVATURE QUADRUPOLE

Let us consider the following expression for the k_x momentum polarization in the $\hat{y}$ direction of a 2D system with a single filled band:

$$P^y_{k_x} = \frac{\Omega}{(2\pi)^2} i\int_{BZ} d^2k k_x \langle u_k | \partial_{k_y} u_k\rangle \equiv \frac{\Omega}{(2\pi)^2} iQ; \quad \text{(D1)}$$

which is just a natural extension of the analogous expression for the charge polarization. We can rewrite the integral denoted as Q as a second moment of the Berry curvature, as we now show. Consider the following quantity:

$$\begin{aligned} F &= -\frac{i}{2}\int_{BZ} d^2k k_x^2 F^{xy} \\ &= \frac{1}{2}\int_{BZ} d^2k k_x^2 \langle \partial_{k_x} u_k | \partial_{k_y} u_k\rangle - \frac{1}{2}\int_{BZ} d^2k k_x^2 \langle \partial_{k_x} u_k | \partial_{k_x} u_k\rangle; \end{aligned} \quad \text{(D2)}$$

where we once again assume F^{xy} to be smooth and integrable in the Brillouin zone spanned by $k_x \in [-\pi/a_x, \pi/a_x)$ and $k_y \in [-\pi/a_y, \pi/a_y)$. Treating the k_x direction of the BZ as open, we integrate by parts with respect to k_x to find

$$\begin{aligned} F &= -\int_{BZ} d^2k k_x \langle \partial_{k_y} u_k | u_k\rangle - \langle \partial_{k_y} u_k | u_k\rangle \\ &\quad - \frac{1}{2}\int_{BZ} d^2k k_x^2 \langle u_k | \partial_{k_x}\partial_{k_y} u_k\rangle \\ &\quad + \frac{1}{2}\int_{BZ} d^2k k_x^2 \langle \partial_{k_x}\partial_{k_y} u_k | u_k\rangle: \end{aligned} \quad \text{(D3)}$$

Note the absence of the Wilson loop contribution we find in the previous section, which is a result of the symmetric nature of the function k_x^2. We see again that the first term is twice the integral of interest $-2Q$. Integrating the third and fourth terms by parts with respect to k_y, we find

$$\begin{aligned} &-\frac{1}{2}\int_{BZ} d^2k k_x^2 \langle \partial_{k_x}\partial_{k_y} u_k | u_k\rangle - \langle \partial_{k_x}\partial_{k_y} u_k | \partial_{k_y} u_k\rangle \\ &= \frac{1}{2}\int_{BZ} d^2k k_x^2 \langle \partial_{k_y} u_k | \partial_{k_x} u_k\rangle - \langle \partial_{k_x} u_k | \partial_{k_y} u_k\rangle \\ &= -\frac{i}{2}\int d^2k k_x^2 F^{yx} = \frac{i}{2}\int d^2k k_x^2 F^{xy} = -F: \end{aligned} \quad \text{(D4)}$$

Summing up, we find

$$\begin{gathered} F = -2Q - F \\ \Downarrow \\ Q = -F; \end{gathered} \quad \text{(D5)}$$

and we find the polarization to be

$$P^y_{k_x} = -\frac{\Omega}{8\pi^2}\int_{BZ} d^2k k_x^2 F^{xy}: \quad \text{(D6)}$$

Performing a similar calculation for $P^x_{k_y}$, we find the general relation

$$P^x_{k_y} = \frac{\Omega}{8\pi^2}\int_{BZ} d^2k k_y^2 F^{xy}: \quad \text{(D7)}$$

APPENDIX E: RESPONSES FOR 1D SYSTEMS

In this appendix,we discuss responses of isolated one-dimensional metals having a fixed number of electrons N_e. For the cases we consider, the Fermi surface consists of an even integer number N_F of Fermi points having chiralities $\chi_a = \mathrm{sgn} v_a$, where v_a is the Fermi velocity of the ath Fermi point. From the fermion doubling theorem [114], the total chirality vanishes: $\chi = \sum_{a=1}^{N_F} \chi_a = 0$. We wish to define three more quantities besides χ that characterize 1D metals:

$$P_x = \sum_{a=1}^{N_F} \chi_a k_{Fx}^{a}, \tag{E1}$$

$$Q_{xx} = \sum_{a=1}^{N_F} \chi_a (k_{Fx}^{a})^2, \tag{E2}$$

$$O_{xxx} = \sum_{a=1}^{N_F} \chi_a (k_{Fx}^{a})^3. \tag{E3}$$

These three quantities represent the momentum space dipole, quadrupole,and octupole moments of the Fermi points, respectively [see Figs. 3(a)–3(c)]. We could go beyond the octupole moment to any higher moment, but for brevity we stop at this order. Importantly, these momentum moments are related to the ground state properties of the metal.The total charge is proportional to the dipole moment:

$$Q = \frac{eL}{2\pi} P_x, \tag{E4}$$

the total momentum $\langle \hbar k_x \rangle$ is proportional to the quadrupole moment:

$$P_x = \frac{1}{2}\frac{\hbar L}{2\pi} Q_{xx}, \tag{E5}$$

the total momentum squared $\langle (\hbar k_x)^2 \rangle$ is proportional to the octupole moment:

$$P_{xx} = \frac{1}{3}\frac{\hbar^2 L}{2\pi} O_{xxx}, \tag{E6}$$

and so on for higher moments. From this, we see that each of the momentum-space moments determines the density of higher and higher powers of momentum, starting at zeroth order where the charge is proportional to the momentum dipole. There are two important caveats to note: (i) In order for the nth moment and its associated physical quantity to be independent of the origin of the BZ, all lower moments must vanish, and (ii) these results hold only up to constants independent of the set of k_{Fx}^{a} which result from contributions from filled bands.

We now want to consider a family of anomalous responses to various gauge fields in 1D metals. We have already considered some of these anomalies in Secs. II B, and we go into more detail in this appendix. To proceed, we introduce a family of gauge fields $e, e^{\alpha}, e^{\alpha\beta}, e^{\alpha\beta\gamma}, \ldots$. Each of these fields couples to charges that are powers of momentum.The field e we identify with the family of electromagnetic gauge field one-forms $(e/\hbar)A$ as it couples to zero powers of momentum. The field e^{α} is the translation gauge field we have extensively discussed, and it couples linearly to momentum k_α. In general, the fields $e^{\alpha\beta\gamma\ldots\zeta}$ couple to the momentum charges $k_\alpha k_\beta k_\gamma \ldots k_\zeta$. Since we consider momentum-space moments only up to the octupole moment O_{xxx}, we consider gauge fields only up to $e^{\alpha\beta\gamma}$.

Using these gauge fields, we can consider the following set of actions:

$$S_\chi = \frac{e^2\chi}{2\pi\hbar}\int d^2r A_0 A_x, \tag{E7}$$

$$S_P = \frac{e}{2\pi}\int d^2r P_x (\partial_0 A_x - e_x^x A_0); \tag{E8}$$

$$S_Q = \frac{\hbar}{2\pi}\int d^2r Q_{xx}\left(\frac{1}{2}e_0^x e_x^x + e(\partial_0 e_0^{xx} A_x - e_x^{xx} A_0)\right); \tag{E9}$$

$$S_O = \frac{\hbar^2}{2\pi}\int d^2r O_{xxx}\left(\frac{1}{3}(\partial_0 e_x^{xx} - e_x^x e_0^{xx}) + e(\partial_0 e^{xxx} A_x - e_x^{xxx} A_0)\right): \tag{E10}$$

These actions capture two important phenomena associated to each of the momentum moments: (i) the connection to the associated ground state quantity, i.e., Q, P_x, and P_{xx}, and (ii) the shift in Q, P_x, P_{xx}, and P_{xxx} when an electric field is turned on. As a first example, let us consider S_χ. We can calculate the electromagnetic charge density and current to find $\rho = (e^2\chi/h) A_x$ and $j^x = (e^2\chi/h) A_0$. If we use these results to calculate the conservation law, we find

$$\partial_\mu j^\mu = \frac{e^2\chi}{h} E_x,$$

which is just the usual U(1) anomaly of a chiral fermion. The fact that $\chi = 0$ for any lattice model has two immediate consequences: (i) The U(1) charge anomaly above vanishes for lattice systems, and (ii) the momentum dipole moment P_x is well defined and independent of the choice of momentum space origin. Just as for conventional electric or magnetic multipole moments, in order for the nth moment to be well defined, all of the lower moments must vanish. As such, the action S_Q is well defined only if $\chi = P_x = 0$. Similarly, for S_O to be well defined, we must have $\chi = P_x = Q_{xx} = 0$.

Now let us consider each of the remaining actions in turn. We begin with S_P. As mentioned in Sec. III B, P_x is related [34] to the charge density of a 1D metal via $\rho = -\delta e/2\pi \partial_x \theta_x$ and the momentum density via $J^0_x = \delta e/2\pi \partial_x A_x$. Assuming that our system is translation invariant, let us consider stretching our system via a time-dependent e_x. During this process, the total number of electrons cannot change. Working from the charge density, we find

$$\partial_t \rho = -\frac{e}{2\pi} \partial_t \delta P_x e_x \quad \text{(E11)}$$

Naively, we are just changing χ, however, if we stretch the system at fixed particle number, the Fermi momenta change inversely. Indeed, we have $\partial_\chi P_x = -\delta P_x / e_x \partial_t e_x$. Inserting this into Eq. (E11), we find

$$\partial_t \rho = -\frac{e}{2\pi} \left(-e_x \frac{P_x}{e_x} \partial_t e_x + P_x \partial_t e_x \right) = 0. \quad \text{(E12)}$$

Using this equation, we find

$$\Delta Q = \int dt \int dx \partial_t \rho = 0 \quad \text{(E13)}$$

as we expect for a fixed number of electrons.

To be self-contained, let us reiterate our argument from the main text. At a fixed particle number, we know the total charge cannot change. Intuitively, we might expect that the density should decrease if we stretch the system. However, the quantity ρ above, which is defined as $\delta S_P / \delta A_0$, is not a scalar density. For general geometries, the scalar charge density would be defined as

$$\bar{\rho} = \frac{1}{e_x} \frac{\delta S}{\delta A_0}. \quad \text{(E14)}$$

To calculate the total charge, we would then use

$$Q = \int dx e_x \bar{\rho} = \int dx \rho. \quad \text{(E15)}$$

Indeed, the scalar charge density $\bar{\rho}$ decreases as the system is stretched, since $\partial_t \bar{\rho} \propto \partial_t P_x$, which decreases as the system size increases at fixed electron number.

Next, we can see that another consequence of a nonvanishing P_x is a mixed crystalline-electromagnetic anomaly. To illustrate this, let us consider the change in momentum density in an applied electric field generated by a change in A_x. We find

$$\partial_t J^x_0 = \frac{e}{2\pi} \partial_t \delta P_x A_x. \quad \text{(E16)}$$

Unlike the previous case, when we turn on a nonvanishing A_x the dipole P_x does not change. Hence, we find the anomalous conservation law

$$\partial_\mu J^\mu_x = \frac{e P_x}{2\pi} E_x. \quad \text{(E17)}$$

Moving on, let us discuss the action S_Q. To have a well-defined quadrupole moment Q_{xx}, we need $P_x = 0$. This scenario can happen nontrivially in systems with more than one occupied band near the Fermi level, as shown in Fig. 3(b). As long as any perturbations we apply keep χ and P_x fixed to zero, then the phenomena associated to Q_{xx} are physically meaningful. From this action, we can derive three separate conservation laws:

$$\partial_t \rho = \frac{e}{2\pi} \partial_t \delta Q_{xx} e_x, \quad \text{(E18)}$$

$$\partial_t J^0_x = \frac{\hbar}{4\pi} \partial_t \delta Q_{xx} e_x, \quad \text{(E19)}$$

$$\partial_t J^0_{xx} = -\frac{e}{2\pi} \partial_t \delta Q_{xx} A_x, \quad \text{(E20)}$$

where the quantities P_x and P_{xx} in Eqs. (E5) and (E6) are determined by $P_x = \int dx J^0_x$ and $P_{xx} = \int dx J^0_{xx}$. The first and third equations generate a kind of mixed anomaly, so let us discuss those first. For fixed electron number, we know that $\partial_t \rho$ must vanish, which implies that $\partial_\chi Q_{xx} = -\delta Q_{xx} / e_x \partial_t e_x$. Thus, the first equation is simply $\partial_\chi \rho = 0$. For the third equation, since changing A_x while keeping $\chi = P_x = 0$ does not change Q_{xx}, we have

$$\partial_\mu J^\mu_{xx} = \frac{e Q_{xx}}{2\pi} E_x. \quad \text{(E21)}$$

This implies that if we insert flux into the system, then the momentum quadrupole moment changes; i.e., the expectation value of the momentum squared in the resulting excited state changes while the total charge and momentum remain fixed.

Returning to the middle equation, we consider the change in momentum as we stretch the system. Crucially, we use the relationship $\partial_t Q_{xx} = -2\delta Q_{xx} / e_x \partial_t e_x$ (heuristically, this comes from the fact that quadratic powers of momentum are proportional to L^{-2}). Inserting this in Eq. (E19), we find

$$\partial_t J^0_x = -\frac{\hbar Q_{xx}}{2\pi} \partial_t e_x + \frac{\hbar Q_{xx}}{4\pi} \partial_t e_x = -\frac{\hbar Q_{xx}}{4\pi} \partial_t e_x.$$

We can interpret the first contribution in the middle section of the above equation as coming from the change in the Fermi points $k^{(a)}_x$ induced by changing e_x. The second contribution arises from the existence of a nonvanishing ground state momentum density when the length of the system is changed. Note that, while the coefficient of the

final result is the same magnitude as Eq. (E19), the sign is opposite. The full conservation law becomes

$$\partial_\mu J^\mu_x = \frac{\hbar Q_{xx}}{4\pi} E^x; \quad \text{(E22)}$$

Finally, if we have a scenario where χ, P_x, and Q_{xx} are all vanishing and remain vanishing after applying any gauge fields, then the phenomena associated to O_{xxx} become physically relevant. Such a scenario can exist in a 1D metal where four bands appear at the Fermi surface [see Fig. 3(c)]. Just as above, let us consider the conservation laws we can derive from O:

$$\partial_t \rho = -\frac{e\hbar^2}{2\pi} \partial_t (O_{xxx} e^{xxx}_x); \quad \text{(E23)}$$

$$\partial_t J^0_x = \frac{\hbar^2}{6\pi} \partial_t (O_{xxx} e^{xx}_x); \quad \text{(E24)}$$

$$\partial_t J^0_{xx} = -\frac{\hbar^2}{6\pi} \partial_t (O_{xxx} e^{x}_x); \quad \text{(E25)}$$

$$\partial_t J^0_{xxx} = \frac{e\hbar^2}{2\pi} \partial_t (O_{xxx} A_x); \quad \text{(E26)}$$

We can use identical arguments as above to determine that $\partial_t O_{xxx} = -(O_{xxx}/e^{xxx}_x)\partial_t e^{xxx}_x$ so that the total charge remains fixed. Under a change of A_x we have $\partial_t O_{xxx} = 0$, and under a change in e^x_x we can determine that $\partial_t O_{xxx} = -3(O_{xxx}/e^x_x)\partial_t e^x_x$. Using these relationships, we can reduce three of the conservation laws to find

$$\partial_\mu j^\mu = 0; \quad \text{(E27)}$$

$$\partial_\mu J^\mu_{xx} = -\frac{\hbar^2 O_{xxx}}{3\pi} E^x; \quad \text{(E28)}$$

$$\partial_\mu J^\mu_{xxx} = -\frac{e\hbar^2 O_{xxx}}{2\pi} E_x. \quad \text{(E29)}$$

To get the final conservation law, we need to determine how O_{xxx} changes when e^{xx}_x changes. From counting powers of length, we find $\partial_t O_{xxx} = -\frac{3}{2}(O_{xxx}/e^{xx}_x)\partial_t e^{xx}_x$. Inserting this into the conservation law for P_x generates

$$\partial_\mu J^\mu_x = \frac{\hbar^2 O_{xxx}}{12\pi} E^{xx}_x. \quad \text{(E30)}$$

In summary, while the anomalous responses we have written in this section are formally correct, it is impossible to uniquely determine the coefficients P_x, Q_{xx}, or O_{xxx} unless all lower moments vanish (starting with the chirality χ). Additionally, even if the lower moments are initially vanishing, turning on gauge fields may generate these moments anomalously and, hence, invalidate the higher moments. We expect that under the assumptions of vanishing lower moments that the highest moment will generate the physical responses described above.

[1] B. I. Halperin, Quantized Hall conductance, current-carrying edge states, and the existence of extended states in a two-dimensional disordered potential, Phys. Rev. B 25, 2185 (1982).

[2] R. B. Laughlin, Quantized Hall conductivity in two dimensions, Phys. Rev. B 23, 5632 (1981).

[3] D. J. Thouless, M. Kohmoto, M. P. Nightingale, and M. den Nijs, Quantized Hall conductance in a two-dimensional periodic potential, Phys. Rev. Lett. 49, 405 (1982).

[4] F. Wilczek, Two applications of axion electrodynamics, Phys. Rev. Lett. 58, 1799 (1987).

[5] X.-L. Qi, T. L. Hughes, and S.-C. Zhang, Topological field theory of time-reversal invariant insulators, Phys. Rev. B 78, 195424 (2008).

[6] J. M. Luttinger, Theory of thermal transport coefficients, Phys. Rev. 135, A1505 (1964).

[7] A. Kapustin and L. Spodyneiko, Thermal Hall conductance and a relative topological invariant of gapped two-dimensional systems, Phys. Rev. B 101, 045137 (2020).

[8] J. E. Avron, R. Seiler, and P. G. Zograf, Viscosity of quantum Hall fluids, Phys. Rev. Lett. 75, 697 (1995).

[9] N. Read, Non-Abelian adiabatic statistics and Hall viscosity in quantum Hall states and $p_x + ip_y$ paired superfluids, Phys. Rev. B 79, 045308 (2009).

[10] M. Sherafati, A. Principi, and G. Vignale, Hall viscosity and electromagnetic response of electrons in graphene, Phys. Rev. B 94, 125427 (2016).

[11] T. L. Hughes, R. G. Leigh, and E. Fradkin, Torsional response and dissipationless viscosity in topological insulators, Phys. Rev. Lett. 107, 075502 (2011).

[12] Y. You, G. Y. Cho, and T. L. Hughes, Response properties of axion insulators and Weyl semimetals driven by screw dislocations and dynamical axion strings, Phys. Rev. B 94, 085102 (2016).

[13] H. Sumiyoshi and S. Fujimoto, Torsional chiral magnetic effect in a Weyl semimetal with a topological defect, Phys. Rev. Lett. 116, 166601 (2016).

[14] J. C. Teo and T. L. Hughes, Topological defects in symmetry-protected topological phases, Annu. Rev. Condens. Matter Phys. 8, 211 (2017).

[15] R. Soto-Garrido, E. Muñoz, and V. Juričić, Dislocation defect as a bulk probe of monopole charge of multi-Weyl semimetals, Phys. Rev. Res. 2, 012043(R) (2020).

[16] S. Laurila and J. Nissinen, Torsional Landau levels and geometric anomalies in condensed matter Weyl systems, Phys. Rev. B 102, 235163 (2020).

[17] O. Dubinkin, F. Burnell, and T. L. Hughes, Higher rank chiral fermions in three-dimensional Weyl semimetals, Phys. Rev. B 109, 115146 (2024).

[18] L. Gioia, C. Wang, and A. A. Burkov, Unquantized anomalies in topological semimetals, Phys. Rev. Res. 3, 043067 (2021).

[19] C. Wang, A. Hickey, X. Ying, and A. A. Burkov, Emergent anomalies and generalized Luttinger theorems in metals and semimetals, Phys. Rev. B 104, 235113 (2021).
[20] J. Nissinen, T. T. Heikkilä, and G. E. Volovik, Topological polarization, dual invariants, and surface flat bands in crystalline insulators, Phys. Rev. B 103, 245115 (2021).
[21] L.-L. Gao, S. Kaushik, D. E. Kharzeev, and E. J. Philip, Chiral kinetic theory of anomalous transport induced by torsion, Phys. Rev. B 104, 064307 (2021).
[22] Y. You, J. Bibo, F. Pollmann, and T. L. Hughes, Fracton critical point at a higher-order topological phase transition, Phys. Rev. B 106, 235130 (2022).
[23] T. Amitani and Y. Nishida, Torsion-induced chiral magnetic current in equilibrium, Ann. Phys. (Amsterdam) 448, 169181 (2023).
[24] M. R. Hirsbrunner, A. D. Gray, and T. L. Hughes, Crystalline-electromagnetic responses of higher order topological semimetals, Phys. Rev. B 109, 075169 (2024).
[25] J. Zak, Berry's phase for energy bands in solids, Phys. Rev. Lett. 62, 2747 (1989).
[26] D. Vanderbilt and R. D. King-Smith, Electric polarization as a bulk quantity and its relation to surface charge, Phys. Rev. B 48, 4442 (1993).
[27] W. A. Benalcazar, B. A. Bernevig, and T. L. Hughes, Quantized electric multipole insulators, Science 357, 61 (2017).
[28] A. M. Essin, J. E. Moore, and D. Vanderbilt, Magnetoelectric polarizability and axion electrodynamics in crystalline insulators, Phys. Rev. Lett. 102, 146805 (2009).
[29] N. P. Armitage and L. Wu, On the matter of topological insulators as magnetoelectrics, SciPost Phys. 6, 46 (2019).
[30] F. D. M. Haldane, Berry curvature on the Fermi surface: Anomalous Hall effect as a topological Fermi-liquid property, Phys. Rev. Lett. 93, 206602 (2004).
[31] A. A. Burkov and L. Balents, Weyl semimetal in a topological insulator multilayer, Phys. Rev. Lett. 107, 127205 (2011).
[32] X. Wan, A. M. Turner, A. Vishwanath, and S. Y. Savrasov, Topological semimetal and Fermi-arc surface states in the electronic structure of pyrochlore iridates, Phys. Rev. B 83, 205101 (2011).
[33] A. A. Zyuzin and A. A. Burkov, Topological response in Weyl semimetals and the chiral anomaly, Phys. Rev. B 86, 115133 (2012).
[34] S. T. Ramamurthy and T. L. Hughes, Patterns of electromagnetic response in topological semimetals, Phys. Rev. B 92, 085105 (2015).
[35] S. T. Ramamurthy and T. L. Hughes, Quasitopological electromagnetic response of line-node semimetals, Phys. Rev. B 95, 075138 (2017).
[36] B. I. Halperin, Possible states for a three-dimensional electron gas in a strong magnetic field, Jpn. J. Appl. Phys., Suppl. 26, 1913 (1987).
[37] L. Fu, C. L. Kane, and E. J. Mele, Topological insulators in three dimensions, Phys. Rev. Lett. 98, 106803 (2007).
[38] Y. Ran, Y. Zhang, and A. Vishwanath, One-dimensional topologically protected modes in topological insulators with lattice dislocations, Nat. Phys. 5, 298 (2009).
[39] P. Zhu, X.-Q. Sun, T. L. Hughes, and G. Bahl, Higher rank chirality and non-Hermitian skin effect in a topolectrical circuit, Nat. Commun. 14, 720 (2023).
[40] B.-J. Yang and N. Nagaosa, Classification of stable three-dimensional dirac semimetals with nontrivial topology, Nat. Commun. 5, 4898 (2014).
[41] B. Bradlyn, J. Cano, Z. Wang, M. G. Vergniory, C. Felser, R. J. Cava, and B. A. Bernevig, Beyond Dirac and Weyl fermions: Unconventional quasiparticles in conventional crystals, Science 353, aaf5037 (2016).
[42] Y. Qi, Z. He, K. Deng, J. Li, and Y. Wang, Multipole higher-order topological semimetals, Phys. Rev. B 109, L060101 (2024).
[43] M.-L. Lu, Y. Wang, H.-Z. Zhang, H.-L. Chen, T.-Y. Cui, and X. Luo, Chiral symmetry protected topological nodal superconducting phase and Majorana Fermi arc, Chin. Phys. B 32, 027301 (2023).
[44] T. Mizoguchi, T. Yoshida, and Y. Hatsugai, Square-root topological semimetals, Phys. Rev. B 103, 045136 (2021).
[45] J. Ahn, D. Kim, Y. Kim, and B.-J. Yang, Band topology and linking structure of nodal line semimetals with Z_2 monopole charges, Phys. Rev. Lett. 121, 106403 (2018).
[46] W. Wu, Y. Liu, S. Li, C. Zhong, Z.-M. Yu, X.-L. Sheng, Y. X. Zhao, and S. A. Yang, Nodal surface semimetals: Theory and material realization, Phys. Rev. B 97, 115125 (2018).
[47] C. K. Chiu, Y. H. Chan, and A. P. Schnyder, Quantized Berry phase and surface states under reflection symmetry or space-time inversion symmetry, arXiv:1810.04094.
[48] N. Manjunath and M. Barkeshli, Classification of fractional quantum Hall states with spatial symmetries, arXiv:2012.11603.
[49] N. Manjunath and M. Barkeshli, Crystalline gauge fields and quantized discrete geometric response for Abelian topological phases with lattice symmetry, Phys. Rev. Res. 3, 013040 (2021).
[50] J. May-Mann and T. L. Hughes, Crystalline responses for rotation-invariant higher-order topological insulators, Phys. Rev. B 106, L241113 (2022).
[51] J. May-Mann, M. R. Hirsbrunner, X. Cao, and T. L. Hughes, Topological field theories of three-dimensional rotation symmetric insulators: Coupling curvature and electromagnetism, Phys. Rev. B 107, 205149 (2023).
[52] J. May-Mann, M. R. Hirsbrunner, L. Gioia, and T. L. Hughes, Crystalline axion electrodynamics in charge-ordered Dirac semimetals, Phys. Rev. B 110, 155110 (2024).
[53] L. D. Landau, L. P. Pitaevskii, E. M. Lifshitz, and A. M. Kosevich, Theory of Elasticity, 3rd ed. (Butterworth-Heinemann, London, 1986).
[54] M. Katanaev and I. Volovich, Theory of defects in solids and three-dimensional gravity, Ann. Phys. (N.Y.) 216, 1 (1992).
[55] M. Vozmediano, M. Katsnelson, and F. Guinea, Gauge fields in graphene, Phys. Rep. 496, 109 (2010).
[56] F. Guinea, M. I. Katsnelson, and A. K. Geim, Energy gaps and a zero-field quantum Hall effect in graphene by strain engineering, Nat. Phys. 6, 30 (2010).
[57] N. Levy, S. Burke, K. Meaker, M. Panlasigui, A. Zettl, F. Guinea, A. C. Neto, and M. F. Crommie, Strain-induced

pseudo-magnetic fields greater than 300 tesla in graphene nanobubbles, Science 329, 544 (2010).
[58] S. Rachel, L. Fritz, and M. Vojta, Landau levels of Majorana fermions in a spin liquid, Phys. Rev. Lett. 116, 167201 (2016).
[59] A. Cortijo, Y. Ferreirós, K. Landsteiner, and M. A. H. Vozmediano, Elastic gauge fields in Weyl semimetals, Phys. Rev. Lett. 115, 177202 (2015).
[60] D. I. Pikulin, A. Chen, and M. Franz, Chiral anomaly from strain-induced gauge fields in Dirac and Weyl semimetals, Phys. Rev. X 6, 041021 (2016).
[61] A. G. Grushin, J. W. F. Venderbos, A. Vishwanath, and R. Ilan, Inhomogeneous Weyl and Dirac semimetals: Transport in axial magnetic fields and Fermi arc surface states from pseudo-Landau levels, Phys. Rev. X 6, 041046 (2016).
[62] T. Matsushita, S. Fujimoto, and A. P. Schnyder, Topological piezoelectric effect and parity anomaly in nodalline semimetals, Phys. Rev. Res. 2, 043311 (2020).
[63] R. Thorngren and D. V. Else, Gauging spatial symmetries and the classification of topological crystalline phases, Phys. Rev. X 8, 011040 (2018).
[64] X.-Y. Song, Y.-C. He, A. Vishwanath, and C. Wang, Electric polarization as a nonquantized topological response and boundary Luttinger theorem, Phys. Rev. Res. 3, 023011 (2021).
[65] T. Kaluza, Zum unitätsproblem der physik, Sitzungsber. Preuss. Akad. Wiss. Berlin (Math. Phys.) 1921, 966 (1921) [Int. J. Mod. Phys. D 27, 1870001 (2018) (translation)].
[66] O. Klein, Quantum theory and five-dimensional theory of relativity (in German and English), Z. Phys. 37, 895 (1926).
[67] D. J. Thouless, Quantization of particle transport, Phys. Rev. B 27, 6083 (1983).
[68] As mentioned, this analogy is precise for gapped systems. For gapless systems, the analogy predicts the correct form of the action but does not uniquely determine the coefficient.
[69] W. P. Su, J. R. Schrieffer, and A. J. Heeger, Solitons in polyacetylene, Phys. Rev. Lett. 42, 1698 (1979).
[70] W. A. Benalcazar, B. A. Bernevig, and T. L. Hughes, Electric multipole moments, topological multipole moment pumping, and chiral hinge states in crystalline insulators, Phys. Rev. B 96, 245115 (2017).
[71] O. Parrikar, T. L. Hughes, and R. G. Leigh, Torsion, parity-odd response, and anomalies in topological states, Phys. Rev. D 90, 105004 (2014).
[72] D. I. Pikulin, A. Chen, and M. Franz, Chiral anomaly from strain-induced gauge fields in Dirac and Weyl semimetals, Phys. Rev. X 6, 041021 (2016).
[73] T. L. Hughes, R. G. Leigh, and O. Parrikar, Torsional anomalies, Hall viscosity, and bulk-boundary correspondence in topological states, Phys. Rev. D 88, 025040 (2013).
[74] B. Bradlyn and N. Read, Low-energy effective theory in the bulk for transport in a topological phase, Phys. Rev. B 91, 125303 (2015).
[75] P. Rao and B. Bradlyn, Hall viscosity in quantum systems with discrete symmetry: Point group and lattice anisotropy, Phys. Rev. X 10, 021005 (2020).
[76] Z. Wang and S.-C. Zhang, Simplified topological invariants for interacting insulators, Phys. Rev. X 2, 031008 (2012).
[77] As shown in the appendix, this anomaly has two contributions. One comes from the low-energy currents that contribute with a factor of $1/2\pi$ and a second from a change of system size for a ground state carrying a nonvanishing momentum density with a factor of $-1/4\pi$.
[78] T. L. Hughes, E. Prodan, and B. A. Bernevig, Inversion-symmetric topological insulators, Phys. Rev. B 83, 245132 (2011).
[79] A. M. Turner, Y. Zhang, R. S. K. Mong, and A. Vishwanath, Quantized response and topology of magnetic insulators with inversion symmetry, Phys. Rev. B 85, 165120 (2012).
[80] Even though there is a $\hat{e}$ wedge product with a lower-dimensional action, it is not transverse to the lower-dimensional action, since $Q_{\alpha\beta}$ is symmetric. For example, there are terms where, say, x couples to de_y, which cannot be interpreted as a conventional stacked action.
[81] Alternatively, we can assume the fields $A^{\alpha}_{w}, e^{\alpha}_{w}$ are locked to their ground state values and, thus, have vanishing derivatives in all directions.
[82] M. Lin and T. L. Hughes, Topological quadrupolar semimetals, Phys. Rev. B 98, 241103(R) (2018).
[83] B. J. Wieder, Z. Wang, J. Cano, X. Dai, L. M. Schoop, B. Bradlyn, and B. A. Bernevig, Strong and fragile topological Dirac semimetals with higher-order Fermi arcs, Nat. Commun. 11, 627 (2020).
[84] M.-C. Chang and Q. Niu, Berry phase, hyperorbits, and the Hofstadter spectrum, Phys. Rev. Lett. 75, 1348 (1995).
[85] M.-C. Chang and Q. Niu, Berry phase, hyperorbits, and the Hofstadter spectrum: Semiclassical dynamics in magnetic Bloch bands, Phys. Rev. B 53, 7010 (1996).
[86] We comment that, even though the Chern-Simons term for the translation gauge fields shares some properties with the electromagnetic Chern-Simons term, there is a key distinction: The translation gauge fields have a constant background. This allows the Dirac-node quadrupole system to have a static momentum polarization, whereas the electromagnetic Chern-Simons term in a Chern insulator would predict generating an electric polarization as one tunes the vector potential.
[87] A. Burkov, Weyl metals, Annu. Rev. Condens. Matter Phys. 9, 359 (2018).
[88] K. Kodama and Y. Takane, Persistent current due to a screw dislocation in Weyl semimetals: Role of one-dimensional chiral states, J. Phys. Soc. Jpn. 88, 054715 (2019).
[89] Z.-M. Huang, L. Li, J. Zhou, and H.-H. Zhang, Torsional response and Liouville anomaly in Weyl semimetals with dislocations, Phys. Rev. B 99, 155152 (2019).
[90] Z.-M. Huang, B. Han, and M. Stone, Nieh-Yan anomaly: Torsional Landau levels, central charge, and anomalous thermal Hall effect, Phys. Rev. B 101, 125201 (2020).
[91] Z.-M. Huang and B. Han, Torsional anomalies and bulk-dislocation correspondence in Weyl systems, arXiv: 2003.04853.
[92] L. Liang and T. Ojanen, Topological magnetotorsional effect in Weyl semimetals, Phys. Rev. Res. 2, 022016(R) (2020).

[93] J. Nissinen and G. E. Volovik, Thermal Nieh-Yan anomaly in Weyl superfluids, Phys. Rev. Res. 2, 033269 (2020).
[94] J. Nissinen and G. Volovik, Tetrads in solids: From elasticity theory to topological quantum Hall systems and Weyl fermions, J. Exp. Theor. Phys. 127, 948 (2018).
[95] J. Nissinen and G. E. Volovik, Elasticity tetrads, mixed axial-gravitational anomalies, and (3 þ 1)-d quantum Hall effect, Phys. Rev. Res. 1, 023007 (2019).
[96] Y. Ferreiros, Y. Kedem, E. J. Bergholtz, and J. H. Bardarson, Mixed axial-torsional anomaly in Weyl semimetals, Phys. Rev. Lett. 122, 056601 (2019).
[97] C.-S. Chu and R.-X. Miao, Chiral current induced by torsional Weyl anomaly, Phys. Rev. B 107, 205410 (2023).
[98] While the coefficient of the response in Eq. (78) is half the size of our numerical and analytic result, our calculations inherently determine the covariant anomaly of the interface Fermi arc states which receives inflow from the bulk term in Eq. (78), i.e., inflow from a boundary term of the same magnitude, hence doubling the result [73,99–101].
[99] C. Callan and J. Harvey, Anomalies and fermion zero modes on strings and domain walls, Nucl. Phys. B250, 427 (1985).
[100] S. G. Naculich, Axionic strings: Covariant anomalies and bosonization of chiral zero modes, Nucl. Phys. B296, 837 (1988).
[101] M. Stone, Gravitational anomalies and thermal Hall effect in topological insulators, Phys. Rev. B 85, 184503 (2012).
[102] M. G. Vergniory, L. Elcoro, Z. Wang, J. Cano, C. Felser, M. I. Aroyo, B. A. Bernevig, and B. Bradlyn, Graph theory data for topological quantum chemistry, Phys. Rev. E 96, 023310 (2017).
[103] B. Bradlyn, L. Elcoro, J. Cano, M. G. Vergniory, Z. Wang, C. Felser, M. I. Aroyo, and B. A. Bernevig, Topological quantum chemistry, Nature (London) 547, 298 (2017).
[104] J. Cano, B. Bradlyn, Z. Wang, L. Elcoro, M. G. Vergniory, C. Felser, M. I. Aroyo, and B. A. Bernevig, Building blocks of topological quantum chemistry: Elementary band representations, Phys. Rev. B 97, 035139 (2018).
[105] J. Cano, B. Bradlyn, Z. Wang, L. Elcoro, M. G. Vergniory, C. Felser, M. I. Aroyo, and B. A. Bernevig, Topology of disconnected elementary band representations, Phys. Rev. Lett. 120, 266401 (2018).
[106] B. Bradlyn, L. Elcoro, M. G. Vergniory, J. Cano, Z. Wang, C. Felser, M. I. Aroyo, and B. A. Bernevig, Band connectivity for topological quantum chemistry: Band structures as a graph theory problem, Phys. Rev. B 97, 035138 (2018).
[107] L. Elcoro, B. J. Wieder, Z. Song, Y. Xu, B. Bradlyn, and B. A. Bernevig, Magnetic topological quantum chemistry, Nat. Commun. 12, 5965 (2021).
[108] Y. Zhang, N. Manjunath, G. Nambiar, and M. Barkeshli, Fractional disclination charge and discrete shift in the Hofstadter butterfly, Phys. Rev. Lett. 129, 275301 (2022).
[109] Z. Gao, M. Hua, H. Zhang, and X. Zhang, Classification of stable Dirac and Weyl semimetals with reflection and rotational symmetry, Phys. Rev. B 93, 205109 (2016).
[110] J. Kim, S. S. Baik, S. W. Jung, Y. Sohn, S. H. Ryu, H. J. Choi, B.-J. Yang, and K. S. Kim, Two-dimensional Dirac fermions protected by space-time inversion symmetry in black phosphorus, Phys. Rev. Lett. 119, 226801 (2017).
[111] A. Kamenev, Course 3 many-body theory of non-equilibrium systems, in Les Houches (Elsevier, New York, 2005), Vol. 81, pp. 177–246.
[112] V. Gurarie, Single-particle Green's functions and interacting topological insulators, Phys. Rev. B 83, 085426 (2011).
[113] J. I. Väyrynen and G. E. Volovik, Soft topological objects in topological media, JETP Lett. 93, 344 (2011).
[114] H. Nielsen and M. Ninomiya, A no-go theorem for regularizing chiral fermions, Phys. Lett. B 105, 219 (1981).